Pion absorption on ^{3}He and ^{4}He with emission of three energetic protons

A. Lehmann,[1,8] D. Androić,[9] G. Backenstoss,[1] D. Bosnar,[9] H. Breuer,[4] H. Döbbeling,[8] T. Dooling,[7] M. Furić,[9] P. A. M. Gram,[3] N. K. Gregory,[5] A. Hoffart,[2,8] C. H. Q. Ingram,[8] A. Klein,[7] K. Koch,[8] J. Köhler,[1] B. Kotliński,[8] M. Kroedel,[1] G. Kyle,[6] A. O. Mateos,[5] K. Michaelian,[8] T. Petković,[9] M. Planinić,[9] R. P. Redwine,[5] D. Rowntree,[5] U. Sennhauser,[8] N. Šimičević,[5] R. Trezeciak,[2] H. Ullrich,[2] M. Wang,[6] M. H. Wang,[6] H. J. Weyer,[1,8] M. Wildi,[1] and K. E. Wilson[5]

(LADS Collaboration)

[1]*University of Basel, CH-4056 Basel, Switzerland*
[2]*University of Karlsruhe, D-76128 Karlsruhe, Germany*
[3]*LAMPF, Los Alamos, New Mexico 87545*
[4]*University of Maryland, College Park, Maryland 20742*
[5]*Massachusetts Institute of Technology, Cambridge, Massachusetts 02139*
[6]*New Mexico State University, Las Cruces, New Mexico 88003*
[7]*Old Dominion University, Norfolk, Virginia 23529*
[8]*Paul Scherrer Institute, CH-5232 Villigen PSI, Switzerland*
[9]*University of Zagreb, HR-41000 Zagreb, Croatia*

(Received 30 January 1997)

Results from a 4π solid angle measurement of the reactions $^3\mathrm{He}(\pi^+,ppp)$ and $^4\mathrm{He}(\pi^+,ppp)n$ at incident pion energies of $T_{\pi^+}=70$, 118, 162, 239, and 330 MeV are presented. For ^{3}He the total absorption cross sections and their decomposition into two-proton and three-proton components are evaluated; for ^{4}He the three-proton absorption cross sections are given. The differential distributions of the three-proton multinucleon absorption mode of both nuclei are analyzed and compared to each other by making use of a complete set of variables. The data are investigated for signatures of initial and final state interactions: it is found that more than half of the three-proton yield cannot be accounted for by cascade mechanisms. The remaining strength shows dependence on the incident pion angular momentum, but also structures that are not explained by simple semiclassical models. [S0556-2813(97)04006-5]

PACS number(s): 25.80.Ls, 25.10.+s, 21.45.+v, 13.75.Gx

I. INTRODUCTION

The existence of a multinucleon pion absorption mode in nuclei is now well established. Several experiments on the three- [1–8] and four- [9,10] nucleon systems have reported final states with three or more nonspectator particles after the absorption of a pion. Measurements on heavier nuclei have given similar results (for a review see Ref. [11]). From these data it is known that the relative strength of the multinucleon absorption mode across the Δ-resonance region is significant and increases with nuclear mass and with incident pion energy. Most of the remainder of the total pion absorption strength originates from the well-known quasifree mode, the absorption on a proton-neutron pair ($2NA$) [12].

Though we have a rough idea about the strength of the multinucleon pion absorption mode, there is still very little knowledge about its origin [11,13]. One important question is how much cascade processes contribute. Both initial state interaction (ISI), where the incident pion scatters on a nucleon before being absorbed by conventional $2NA$, and final state interaction (FSI), where one of the outgoing nucleons of $2NA$ interacts with another nucleon in the nucleus, can lead to three energetic particles in the final state ($3NA$). Despite focused searches for direct signatures of such cascade mechanisms in ^{3}He [5,14], until recently [15,16] no significant strength was observed. In Ref. [15] only a part of the multinucleon yield is explained in terms of an ISI process, and so the major question remains: Does there exist a mechanism in which the pion is coherently absorbed on more than two nucleons?

Theoretical examples of such processes are the ''alpha-pole model'' [17] or the ''double-delta'' mechanism [18], both of which involve four nucleons. Similar mechanisms have been constructed for three nucleons [19]. But even more exotic processes have been considered. For example, Fasano and Lee [20] approach the three-nucleon force as an interaction of a six-quark bag with a nucleon. Assuming the six-quark bag to be an excitation of a πNN system, this gives a direct relation between $3NA$ and the three-nucleon force.

Past experiments on the light systems suffered from limitations in phase space coverage, kinematic definition, or statistical accuracy for the multinucleon channels. Hence investigations of differential distributions did not reveal details which might signal specific dynamics. The common result of these studies was that the outgoing particles of the $3NA$ process were distributed uniformly over $3N$ phase space.

A very interesting question is how the $3NA$ mode, first observed in the three nucleon system, appears in heavier nuclei. The lightest nucleus in this context is ^{4}He. Investigation on this nucleus is also important because the final states can be measured kinematically completely for most configurations. Furthermore, while for π^+ absorption there is only one final state in ^{3}He: ppp, there are two important ones in ^{4}He: $pppn$ and ppd. A thorough investigation of the cross sections and distributions of these final states should give

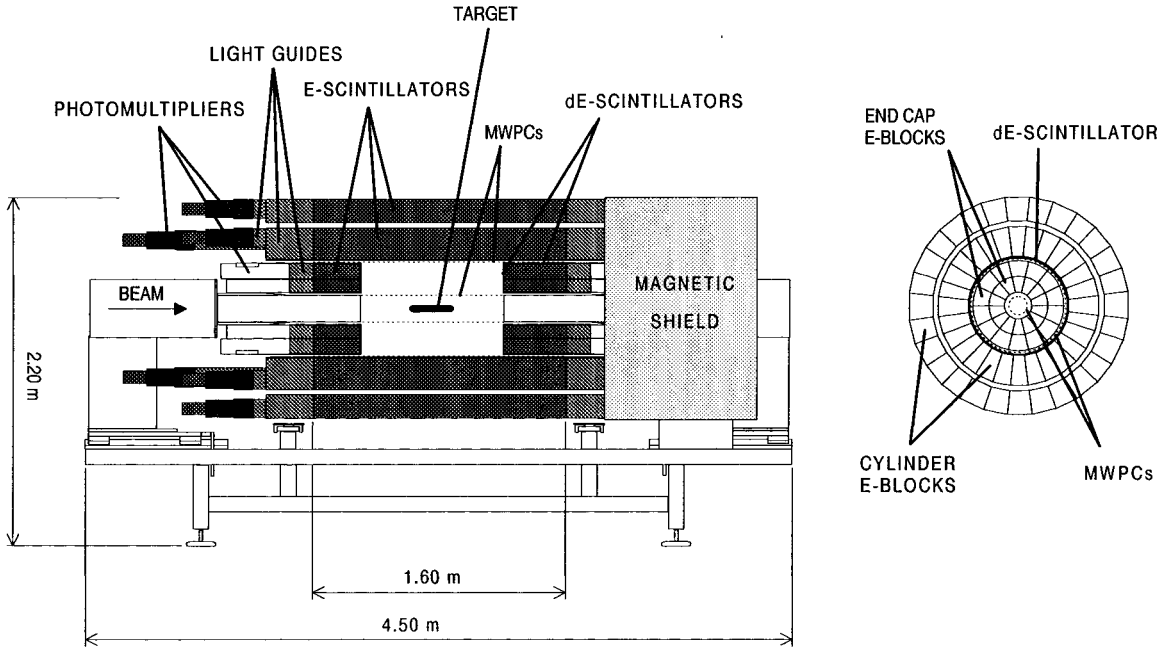

FIG. 1. A schematic view of the LADS detector.

more knowledge about the contribution of cascade processes to the multinucleon strength. From the different nuclear environment one would also anticipate modifications like broadening of signatures or changes in the relative importance of mechanisms such as ISI and FSI. After these processes are taken into account, examination of the differential distributions may indicate if there is a common source for the remaining yield. In particular, a coherent $3NA$ process might show similar features in all distributions from nuclei with $A \geqslant 3$. The additional step to address this issue is the comparison of the $(ppp)n$ channel in ^{4}He, where the neutron acted as a spectator, to the (ppp) channel in ^{3}He.

This paper deals with results for the three-nucleon absorption on ^{3}He and ^{4}He, for incident positive pions at 70, 118, 162, 239, and 330 MeV, resulting in three energetic protons measured with a 4π solid angle detector. Some of the results on ^{3}He have been reported earlier [7,15]. The $3NA$ distributions of the reaction $^3\mathrm{He}(\pi^+,ppp)$ will be investigated in more detail and compared to the analogous reaction $^4\mathrm{He}(\pi^+,ppp)n$.

II. EXPERIMENT

The measurements were performed with the Large Acceptance Detector System (LADS) (see Fig. 1 and Ref. [21]) which was built at the Paul Scherrer Institute (PSI) in Villigen, Switzerland, to investigate in particular multinucleon pion absorption. With the large solid angle coverage of more than 98% of 4π and the low proton kinetic energy threshold of $T_{\mathrm{thr}} \approx$ 20 MeV, a large fraction of the phase space was accessible to LADS even at low incident pion energies.

The detector consisted of a plastic scintillator cylinder divided into 28 $\Delta E-E-E$ sectors, each 1.6 m in active length. The ends of the cylinder were closed by ''end caps,'' each consisting of 14 $\Delta E-E$ plastic scintillator sectors. The scintillators stopped normally incident protons of up to 250 MeV, and measured their energy with an overall resolution of about 3% FWHM. The trajectory information for charged particles was provided by two coaxial cylindrical multiwire proportional chambers (MWPC's) inside the plastic cylinder. Their angular resolution was about 1° FWHM. The target was a high pressure (up to 100 bars) gas cylinder of 25.7 cm length and 2 cm radius with carbon-fiber/epoxy walls of 0.5 mm thickness to keep background and particle thresholds low. A multicoincidence trigger logic allowed specific final states of interest to be emphasized dependent on their charged or neutral multiplicities.

The π^+ beam was defined by a set of plastic scintillation detectors (BEAM) that counted the individual pions and removed particles in the beam halo. Some 5% of the typical incident flux of about 10^6 momentum-analyzed pions per second was finally accepted by a 2 cm diameter scintillator placed about 50 cm upstream of the target center.

III. DEFINITION OF KINEMATIC QUANTITIES

A. Independent variable set

For the complete description of a known three-body final state, five independent variables are required. It is convenient to work in the center-of-mass (c.m.) system of the three outgoing particles, because their momentum vectors form a plane in this frame. The orientation of the c.m. system in space with respect to the laboratory (lab) frame gives a straightforward definition of three independent variables, the Euler angles, with the incident pion beam determining the z coordinate axis.

The angle between the normal $\hat{n}$ of the c.m. plane and the beam axis is defined as the plane angle, ξ. The distribution over ξ reflects the total angular momentum of a three-body

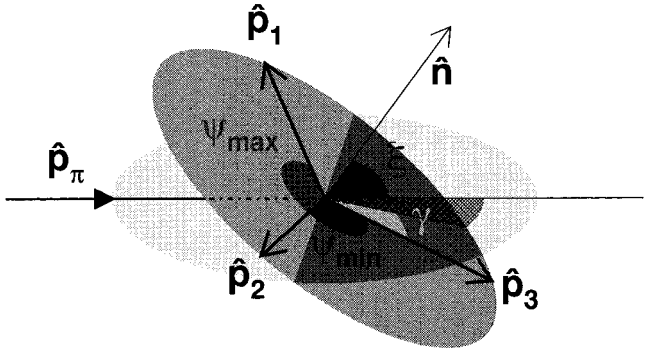

FIG. 2. Scheme to illustrate the definition of the independent variable set (see text for description of the variables). The angle β, not shown in the scheme, is the azimuth of the normal $\hat{n}$ to the c.m. plane around the beam axis. The two ellipses are an illustration of this c.m. plane in-plane (horizontal) and out-of-plane (tilted).

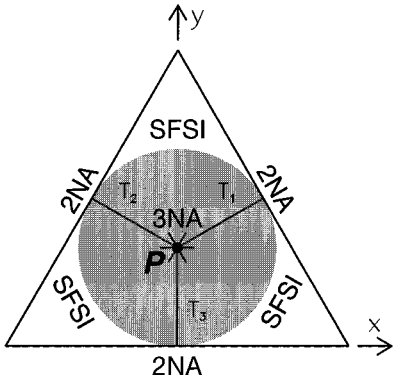

FIG. 3. Schematic of a triangular Dalitz plot. The kinetic energies of each event are completely determined by a point [e.g., P at $(x,y)=(0,0)$] inside the shaded area which shows the kinematically allowed region; particle thresholds cut from the legs of the triangle. The regions expected to be populated by specific mechanisms ($2NA$, SFSI [for definition see Sec. IV B and Sec. V B]) are labeled at the boundary of the Dalitz plot (threefold because of symmetry). $3N$ phase space ($3NA$) uniformly fills the shaded area.

system [22–24], analogously to the distribution over the polar angle in two-body reactions. The orientation of the protons within the plane is specified by the angle between one particle (which we take to be that with the lowest energy) and the projection of the beam axis onto the plane. This angle will be referred to as the rotation angle, γ. The final Euler angle, the azimuth of the normal $\hat{n}$ around the beam axis, we will call β. Because there was no polarization measurement in the experiment the events must be uniformly distributed over this angle.

An additional two independent variables are necessary to specify the final state completely. We choose the maximum and minimum opening angles between the three particles in their c.m. plane, $\psi_{\max}$ and $\psi_{\min}$. The definitions of the four nontrivial variables are illustrated in Fig. 2.

If $\hat{\mathbf{p}}_1$, $\hat{\mathbf{p}}_2$, and $\hat{\mathbf{p}}_3$ are the unit vectors of the outgoing particle momenta in the three-body c.m. system ($T_1>T_2>T_3$; $T_i :=$kinetic energy of particle i), $\hat{\mathbf{p}}_\pi$ the unit vector of the incident pion momentum in the lab, and $\hat{\mathbf{n}}=\hat{\mathbf{p}}_2\times\hat{\mathbf{p}}_1/|\hat{\mathbf{p}}_2\times\hat{\mathbf{p}}_1|$ the normal to the plane spanned by the three particles, then the independent variables are formally defined as follows:

$$\beta=\arctan\frac{n_y}{n_x}, \tag{3.1}$$

$$\xi=\arccos(|\hat{\mathbf{p}}_\pi\cdot\hat{\mathbf{n}}|), \tag{3.2}$$

$$\gamma=\arccos\left(\hat{\mathbf{p}}_3\cdot\frac{\hat{\mathbf{n}}\times(\hat{\mathbf{p}}_\pi\times\hat{\mathbf{n}})}{|\hat{\mathbf{n}}\times(\hat{\mathbf{p}}_\pi\times\hat{\mathbf{n}})|}\right), \tag{3.3}$$

$$\psi_{\min}=\arccos(\hat{\mathbf{p}}_3\cdot\hat{\mathbf{p}}_2), \tag{3.4}$$

$$\psi_{\max}=\arccos(\hat{\mathbf{p}}_2\cdot\hat{\mathbf{p}}_1). \tag{3.5}$$

B. Dalitz plot

An alternative independent variable set consists of the three Euler angles β, γ, ξ together with the two kinetic energies T_1 and T_2. Using the total kinetic energy in the three-particle c.m. system, $Q=T_1+T_2+T_3$, a highly symmetric representation of the data can be defined: the triangular Dalitz plot (Fig. 3). The complete energy related kinematics of an event (e.g., at point P in Fig. 3) is expressed in terms of the two coordinates $x=(T_1-T_2)/\sqrt{3}$ and $y=T_3-Q/3$.

A well-known property of the triangular Dalitz plot is its constant event density in phase space and its correlation to angular configurations of the particles. Particle detection thresholds impinge on the experimentally accessible region from the sides of the triangle, but do not modify the interior region. A more detailed discussion about the different absorption mechanisms and their population of Dalitz plot regions can be found in Ref. [4].

IV. DATA ANALYSIS

A. Data treatment

The vertex of each event was reconstructed with the trajectory information measured by the MWPC's. Only events with track information for all charged particles, and thus a well-defined vertex, were accepted. The spatial vertex resolution of about 1 mm FWHM allowed a very efficient elimination of background events originating in the target walls (see Fig. 4). Only events inside a volume of 100 mm upstream and downstream of the target center and 17 mm around the beam axis were used. Measurements with empty targets indicated that these cuts reduced the wall background to less than 4% for the 70 MeV ppp events of ^{4}He, which was the worst case because of a wide beam and the low ppp cross section. For the other energies this background was considerably less.

The data of each individual scintillator channel were calibrated to have the same gain and timing [21]. After correction for small nonlinearities in the analogue branch a total energy resolution of about 3% FWHM could be achieved. Together with the MWPC's angular resolution of roughly 1° FWHM, this gave a reconstructed missing mass resolution for three protons of about 8 MeV, and of about 15

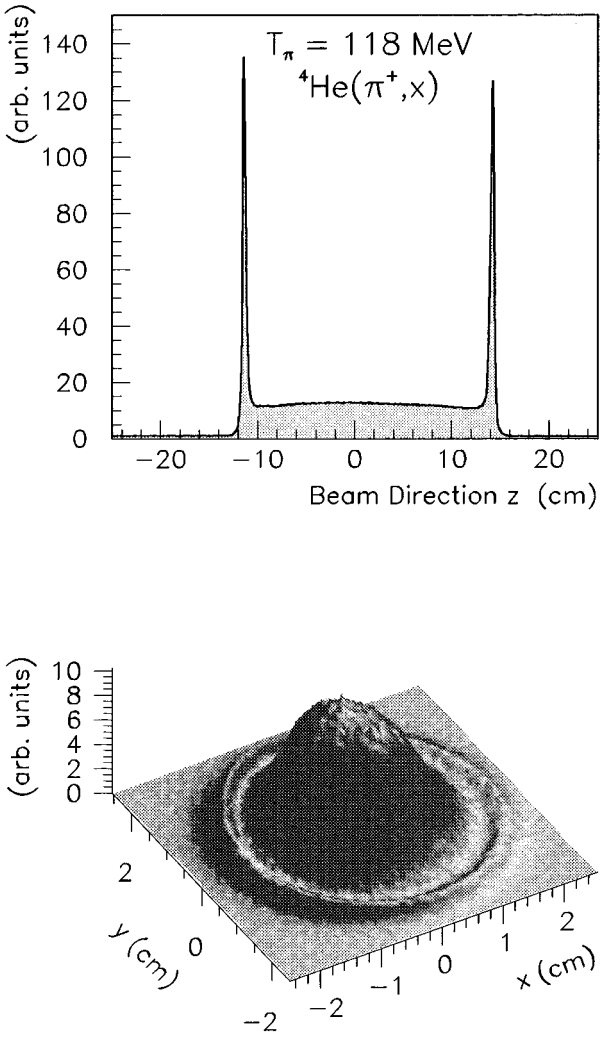

FIG. 4. Vertex reconstruction plots with the target cell filled with ^{4}He gas. Upper: For the projection in the beam direction (z) a radial cut of 17 mm was applied. The two sharp peaks reflect background events from the target wall end caps. Lower: For the projection onto the transverse ($x-y$) plane a cut of 10 cm upstream and downstream of the target center was applied. The events from the target gas (broad bump) can be clearly distinguished from those of the target walls (ring around the center).

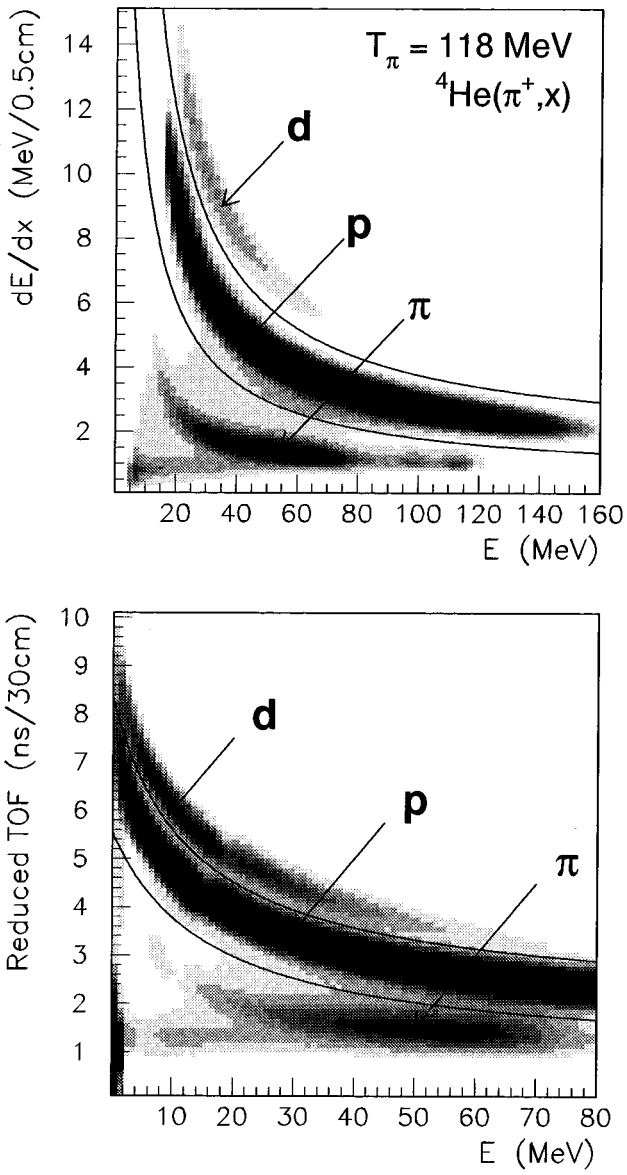

FIG. 5. $E-dE/dx$ (upper) and E-TOF (lower) spectra used for the particle identification. The kinks around 20 MeV in the lower plot are caused by the transition from the ΔE to the E scintillators. The cuts applied for proton selection are also shown (solid curves).

MeV/c in missing momentum.

For the separation of protons from other particles like pions and deuterons, conventional $E-dE/dx$ and E-TOF (time-of-flight) particle identification (PID) techniques were applied. The latter was used for all charged particles with less than about 10 MeV energy deposit in the E scintillators, because these were stopped in or just passed through the thin ΔE counters. Figure 5 indicates the reliability of these methods for reactions on ^{4}He. The same proton separation cuts, indicated by the solid curves, were applied in the ^{3}He analysis.

In the next step only events with three protons and no identified charged pion were selected. In the case of ^{4}He all events with three protons with and without an additional identified neutron were accepted. A cut on the reconstructed missing mass of ± 15 MeV around the peak center removed most of the background events originating from remaining pionic final states, mainly due to single charge exchange, which are separated by about the pion mass. Furthermore, most events where a proton underwent a nuclear reaction in the scintillator material and lost a part of its energy were rejected by this cut.

For both ^{3}He and ^{4}He all three proton energies and angles were taken to be those given by the detector. For ^{4}He this information was used to reconstruct the neutron's mass and momentum, whether or not the neutron was also detected; this provided better angle and energy resolution than given by the detector directly.

To eliminate events near the edge of the detector acceptance the polar angular range of the data was limited between 15° and 165°. With this cut the covered solid angle was slightly reduced to 96.6% of 4π.

TABLE I. Summary of event generators used for the reactions $^3\mathrm{He}(\pi^+,ppp)$ and $^4\mathrm{He}(\pi^+,ppp)n$. More detailed descriptions of the abbreviations are given in the text. All σ's are differential cross sections as a function of the polar scattering angle. The ρ's are momentum density distributions, the F's are Jost enhancement functions.

Nucleus	Event generator	Weighting factors
^{3}He	$3NA^{L\geq 0}_{(ppp)}$	$3NA_{(ppp)} * P_0[\cos(\xi)] * F_{pp}$
	$3NA^{L\geq 1}_{(ppp)}$	$3NA_{(ppp)} * \{1-P_2[\cos(\xi)]\} * F_{pp}$
	$2NA_{(pp)p}$	$3NA_{(ppp)} * \rho_p * \sigma_{2NA} * F_{pp}$
	$\mathrm{ISI}_{(ppp)}$	$\rho_p * \sigma_{\pi p} * \sigma_{2NA} * F_{pp}$
	$\mathrm{HFSI}_{(ppp)}$	$\rho_p * \sigma_{2NA} * \sigma_{pp} * F_{pp}$
^{4}He	$4NA_{(pppn)}$	$4NA_{(pppn)} * F_{pp} * F_{pn}$
	$3NA_{(ppn)p}$	$4NA_{(pppn)} * \rho_N * F_{pp} * F_{pn}$
	$3NA^{L\geq 0}_{(ppp)n}$	$4NA_{(pppn)} * \rho_N * P_0[\cos(\xi)] * F_{pp} * F_{pn}$
	$3NA^{L\geq 1}_{(ppp)n}$	$4NA_{(pppn)} * \rho_N * \{1-P_2[\cos(\xi)]\} * F_{pp} * F_{pn}$
	$2NA_{(pp)pn}$	$4NA_{(pppn)} * \rho_N * \rho_N * \sigma_{2NA} * F_{pp} * F_{pn}$
	$\mathrm{ISI}_{(ppp)n}$	$\rho_N * \rho_N * \sigma_{\pi p} * \sigma_{2NA} * F_{pp} * F_{pn}$
	$\mathrm{HFSI}_{(ppp)n}$	$\rho_N * \rho_N * \sigma_{2NA} * \sigma_{pp} * F_{pp} * F_{pn}$

After all these cuts the ^{3}He data were clean, but a small background (about 2–3 %) from deuteronic final states remained in the ^{4}He data, where the deuteron was misidentified as a proton. For such events the reconstructed ''neutron'' is parallel to the misidentified proton. This background was removed by rejecting events in which the reconstructed neutron angle was within 8° of one of the protons. This cut also rejected some events with strongly correlated proton-neutron pairs from the SFSI mechanism (for definition see Sec. IV B and Sec. V B), but these were corrected for in the final evaluation of the cross sections.

B. Monte Carlo simulations

Monte Carlo simulations were made to correct for the acceptance and inefficiencies of the detector and to assist the physics interpretation of the data. For all simulations, the particles were tracked through a model of the detector using the CERN GEANT software package. The simulated data were then treated with the same analysis program as used for the real data. The experimental resolutions and hardware thresholds, as determined from the data for each scintillation counter and MWPC, were applied to the simulated raw events. The effects of geometrical acceptance, energy thresholds, and reaction losses in the detector, as well as inefficiencies of the chambers and the reconstruction code, were thus reflected in the simulated particle distributions in the same way as in those of the experimental data. The reliability of this procedure was tested in many ways and is discussed in detail elsewhere [15,25–27].

(a) ^{3}He: Five different event generators, three one-step and two two-step, were used for the reaction $^3\mathrm{He}(\pi^+,ppp)$ (see Table I): The simplest one-step generator created final states with three nucleons ($3N$) uniformly distributed over phase space ($3NA_{(ppp)}$). The events of this generator were additionally weighted by the Legendre polynomials $P_0[\cos(\xi)]$ and $\{1-P_2[\cos(\xi)]\}$ to reflect components from total initial orbital angular momentum $L\geq 0$ ($3NA^{L\geq 0}_{(ppp)}$) and $L\geq 1$ ($3NA^{L\geq 1}_{(ppp)}$), respectively, as proposed by Šimičević and Mateos [28]. The third one-step generator ($2NA_{(pp)p}$) modeled the two-nucleon absorption on a quasideuteron in ^{3}He. In this model the momentum distribution (ρ_p) of the spectator proton was taken from a calculation [29] based on $^3\mathrm{He}(e,e'p)d$ data [30] and the differential cross section for absorption on a deuteron (σ_{2NA}) was obtained from a parametrization of experimental data [31]. With the two-step generators, distributions from (ISI+$2NA$) and ($2NA$+HFSI) (HFSI is hard final state interaction) cascade processes were simulated in simple semiclassical models. In the ISI model ($\mathrm{ISI}_{(ppp)}$), the incident pion was first scattered by one proton (with a momentum distribution given by ρ_p), according to the elastic πN cross section ($\sigma_{\pi p}$) calculated with the phase shift code SCATPI [32], before being absorbed on the recoiling quasideuteron according to the deuteron cross section (σ_{2NA}). The suppression of the forward pion quasielastic cross section due to the proton's binding energy was treated with a weighting factor that fell linearly from unity to zero for 500 MeV/c and stationary protons, respectively. In the HFSI simulation ($\mathrm{HFSI}_{(ppp)}$), the pion was first absorbed on the quasideuteron moving with the initial momentum opposite to that of a proton (ρ_p), and then one of the outgoing protons was scattered off the remaining proton according to its elastic NN cross section (σ_{pp}), calculated with the program SAID [33]; a minimum momentum transfer of 150 MeV/c was required in this case. In both cascade models the energy needed to break up the nucleus was included in the kinematics of the absorption step.

(b) ^{4}He: For the reaction $^4\mathrm{He}(\pi^+,ppp)n$ seven different event generators, five one-step and two two-step, were found to be necessary (see Table I): In the simplest case events with three protons and one neutron ($4N$) were generated with constant density in phase space ($4NA_{(pppn)}$). There are two possible $3NA$ modes in the $pppn$ final state of ^{4}He: $(ppn)p$ and $(ppp)n$. The first one ($3NA_{(ppn)p}$) was modeled with a $4N$ phase space distribution ($4NA_{(pppn)}$), where one proton was weighted with a momentum distribution (ρ_N), calculated by Schiavilla [34,35] to fit $^4\mathrm{He}(e,e'p)^3\mathrm{H}$ data [36]. The second mode ($3NA_{(ppp)n}$) was simulated

similarly, assuming the spectator neutron to have the same momentum distribution as a proton. As for ^{3}He, in these events the ppp subsystem was additionally weighted with Legendre polynomials to take into account angular momentum effects ($3NA^{L\geq 0}_{(ppp)n}$, $3NA^{L\geq 1}_{(ppp)n}$). The quasifree $2NA$ mode was treated as in ^{3}He, using the differential deuteron absorption cross section (σ_{2NA}), and with the neutron and one proton of the $4N$ phase space ($4NA_{(pppn)}$) being weighted to be independent spectators (ρ_N). Besides kinematics and binding energy the ISI and HFSI cascade generators ($\mathrm{ISI}_{(ppp)n}$, $\mathrm{HFSI}_{(ppp)n}$) for ^{4}He differed from those of ^{3}He only by an additional momentum distribution weight for the spectator neutron (ρ_N).

Finally, each nucleon pair of the described event generators was additionally weighted with the Jost enhancement functions F_{pp} and F_{pn} [37–39] to take into account the Watson-Migdal type soft final state interaction (SFSI) [40]. This is a well-known coherent effect that increases the cross section of those kinematical configurations where the relative momentum of two nucleons is very small. For proton-neutron SFSI an effective range of $r_0=2.60$ fm and a scattering length of $a=-23.7$ fm were taken. The respective parameters for proton-proton SFSI were $r_0=2.66$ fm and $a=-7.70$ fm.

C. Fits and efficiency correction

Monte Carlo histograms for all event generators were generated in three different ways.

LADSON30: These histograms contained events which survived the full simulation of the detector's acceptance and efficiency including all software cuts applied in the analysis of the data. Thus all experimental losses and resolutions were taken into account. In addition, a threshold of 30 MeV was applied to all three protons; this rejected most of the $2NA$ events (with one spectator proton) leaving predominantly those from $3NA$.

LADSOFF30: These histograms were formed from the simulated events at the interaction vertex without any detector restrictions or cuts applied except that all protons were required to be above 30 MeV kinetic energy.

LADSOFF0: These distributions were the same as LADSOFF30, but without the minimum kinetic energy requirement.

In a first step the LADSON30 distributions of the different event generators were fitted to the real data ($T_p > 30$ MeV) with the normalizations as free parameters. This was done by simultaneous fits to various histogram sets with the CERNLIB routine MINUIT: the five independent variables (β, γ, ξ, $\psi_{\min}$, $\psi_{\max}$), a set of selected one-dimensional distributions (proton polar angle θ_p, momentum of the least energetic proton p_3, pseudoinvariant mass squared m_x^2 [41], proton-proton invariant mass M_{pp}, proton-proton opening angle in lab ψ_{pp}) and a set of two-dimensional histograms with pronounced correlations (θ_p vs p_3, m_x^2 vs p_3, m_x^2 vs θ_p). In addition, fits using all these distributions together were made.

The maximum allowed yield of some event generators, where only the tails of the spectator momentum distributions survived the applied cuts and thresholds, had to be fixed. This was because the resulting small, but not negligible, contributions to the investigated ppp data sample were not well constrained in the fits. In these cases the contributing fractions [of, e.g., $(ppn)p$ events in the $(ppp)n$ channel] were determined from the partial cross sections, evaluated from the same data and published elsewhere [7,25]. These event generators were $2NA_{(pp)p}$ for ^{3}He and $4NA_{(pppn)}$, $3NA_{(ppn)p}$ and $2NA_{(pp)pn}$ for ^{4}He.

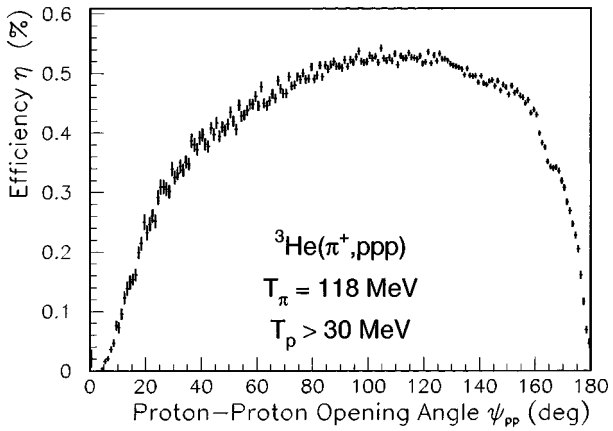

FIG. 6. Differential efficiency for the proton-proton opening angle ψ_{pp} in the laboratory system. The steep falloff at low and high angles is mainly caused by the finite segmentation of the detector.

In a second step the differential efficiencies $\eta_i(x)$ for each simulated mechanism i and variable x were determined according to

$$\eta_i(x)=\frac{\mathrm{LADSON30}_i(x)}{\mathrm{LADSOFF30}_i(x)}. \tag{4.1}$$

Regions with $\eta_i(x)<1\%$ were removed. The efficiency corrected histograms were finally obtained with the formula

$$N(x)=\sum_i p_i \frac{\sum_{j=1}^{8} a_j N_j(x)}{\eta_i(x)} \tag{4.2}$$

with p_i the fitted normalization parameters, $N_j(x)$ the histogram channel content per trigger type j of the real data and a_j its corresponding prescale factor [21] corrected for deadtime.

In Fig. 6 a typical example of a differential efficiency, weighted according to the proportions of each mechanism found in the fit to the data, is shown as a function of the proton-proton opening angle. In this plot all losses caused by the reconstruction code, the MWPC's, reaction losses in the scintillators, uncovered acceptance, etc., are reflected. It becomes clear from this plot that the differential efficiency has to be determined for each investigated variable individually. However, the average efficiency integrated over all events is of the order of 50%, varying slightly with the incident pion energy. Even when an extrapolation to zero threshold is made (LADSON30/LADSOFF0) this average efficiency remains of the order of 30%.

This method of efficiency correction was also applied for the 330 MeV data. For this incident pion energy the most energetic protons after the absorption process may not be

stopped by the scintillators and their kinetic energy is thus underestimated. This typically causes a rejection of the event by the PID or reconstructed missing mass cuts. Detailed investigations on ^{3}He [42] using only the six measured angles of the ppp final state events to reconstruct the protons' kinetic energies gave the same physics results and thus showed that losses due to this ''punch-out'' effect were reliably taken into account in the Monte Carlo simulations.

In this paper, only differential cross sections corrected for the efficiency will be shown in the figures (usually with $T_p > 30$ MeV and $p_n < 200$ MeV/c for ^{4}He), often together with the LADSOFF30 distributions weighted according to the mean fractions of the fits to the various sets. The error bars of the data points in the histograms reflect the statistical uncertainties of the raw data and the simulations.

The cross sections cited in this paper for thresholds of 20 MeV and 30 MeV are mean values from the fits to the different histogram sets. The error is taken as half the difference between the maximum and minimum values. The total and partial cross sections for zero threshold are mean values of extrapolations from fits to the various histogram sets with detector, 20 MeV and 30 MeV thresholds. The error bars are the corresponding standard deviations of the results from the various fits. To test the model dependence of the results fits were also made with modified HFSI and ISI simulations, but the cross sections were usually inside the error bars obtained with the above-mentioned methods.

D. Normalization

To evaluate the absolute normalization of the cross sections, differential and integrated, the number of incident pions and target nuclei had to be determined and corrections for efficiency and acceptance losses had to be applied.

First the numbers N_j of recorded events per trigger type (for more detailed information see Ref. [21]) were scaled with their deadtime corrected prescale factors. Then the number of incident pions $N_{\rm BEAM}$ was corrected for the fraction which decay or react on their way from the beam defining counter to the target and for the number of pions which miss the target entirely. A correction was also made for the amount of contamination in the beam and the efficiency of the beamline hodoscope. Where possible these correction factors were determined from the data [25,26,43]. Its high pressure made it necessary to treat the helium as a real gas and include compression effects in the calculation of the number of scatterers $N_{\rm scat}$. Finally, all cross sections were corrected for efficiency losses in the way described in the previous paragraph.

In summary the differential cross section over a variable x was calculated from the expression

$$\frac{d\sigma}{dx} = \frac{N(x)}{N_\pi \cdot N_{\rm scat}} \tag{4.3}$$

with $N(x)$=histogram entry as determined in previous section; $N_\pi = N_{\rm BEAM}\cdot(1-f_\mu)\cdot(1-f_{sb})\cdot(1-f_r)\cdot(1-f_d)\cdot(1-f_m)\cdot f_h$; $N_{\rm scat} = (\rho_{\rm real}\cdot N_L \cdot n/M)\cdot l_{\rm tgt}$; $N_{\rm BEAM}$:=number of counts passing the BEAM logic; f_μ:= fraction of muons in the beam; f_{sb}:=fraction of pions that reacted in the beam defining counter; f_r:=fraction of pions that reacted in the material between the beam counter and the target center; f_d:=fraction of pion decays from beam counter to target center; f_m:=fraction of counted pions missing the target due to multiple scattering; f_h:=efficiency of the beamline hodoscope; $\rho_{\rm real}$:=density of the target gas (real gas); N_L:=Avogadro constant; n:=number of nuclei/target gas molecule; M:=target gas molecular weight; $l_{\rm tgt}$:=target length.

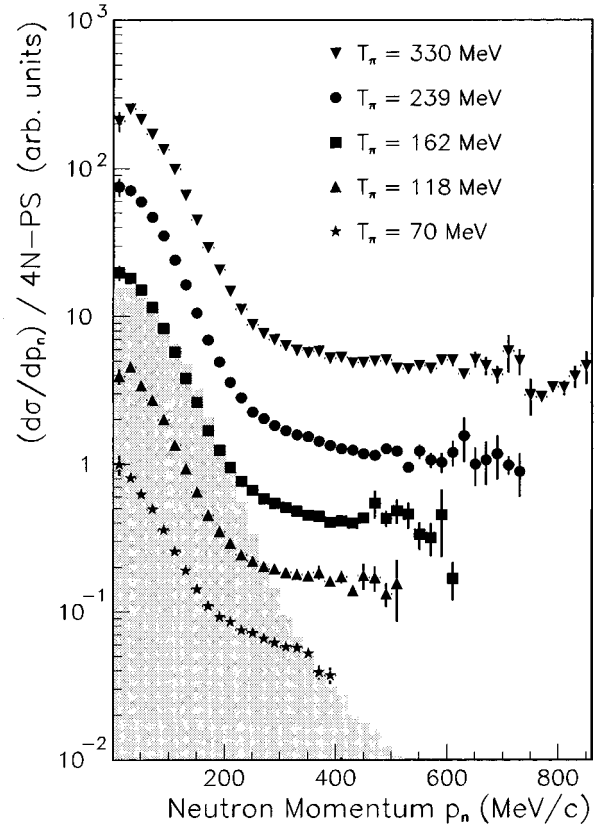

FIG. 7. Momentum density distribution of the neutron from the reaction ^{4}He$(\pi^+,ppp)n$ with $T_p > 30$ MeV for five incident pion energies, divided by a $4N$ phase space simulation ($4NA_{(pppn)}$). The solid points are the data, arbitrarily normalized, while the shaded area represents a Monte Carlo $3NA^{L\geq 0}_{(ppp)n}$ simulation at 162 MeV where the neutron was weighted to be a spectator.

All integrated cross sections cited in this paper were corrected for the overall average detector efficiency, which was obtained directly for each simulation from the homogeneous efficiency distributions of the independent variable β.

V. RESULTS

A. Final states

As already mentioned, the absorption of a positive pion in ^{3}He leads to only one final state: ppp. Consequently there is only one possible $3NA$ mode. The situation becomes richer in ^{4}He, where three final states, $pppn$, ppd, and a weak p^3He are accessible. The final state of interest for this paper, $pppn$, can be further classified according to three multinucleon modes: $(pppn)$, a $4NA$ mode where all four nucleons are somehow involved in the absorption process; and the two isospin-different $3NA$ modes $(ppn)p$ and $(ppp)n$, the

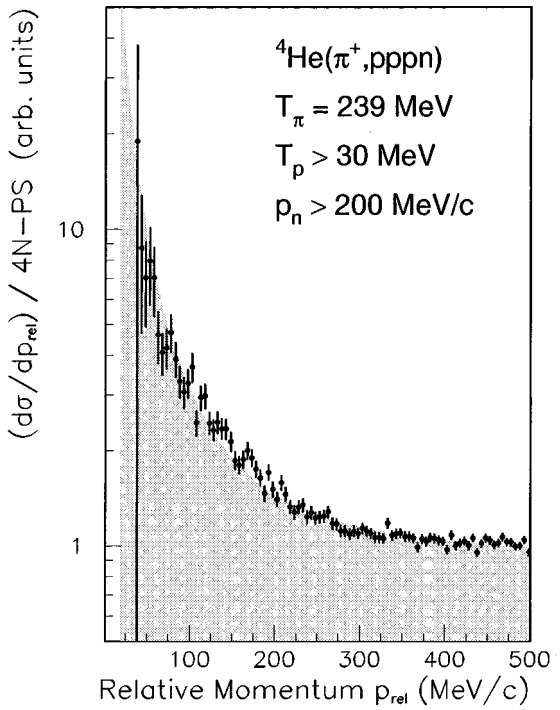

FIG. 8. Measured relative momentum of proton-neutron pairs from the reaction ^{4}He(π^+,$pppn$) at 239 MeV divided by a LADSON30 $4NA_{(pppn)}$ simulation. The shaded area represents the Jost pn-SFSI enhancement function.

analogous mode to (ppp) on ^{3}He, with one nucleon acting as spectator. The partial cross sections of these modes and of the additional absorption channels, as, e.g., $2NA$, can be found elsewhere [7,25].

Besides the Q value and nucleon density, the reaction ^{4}He(π^+,$pppn$) differs from that of ^{3}He(π^+,ppp) by additional degrees of freedom introduced by the presence of the neutron. The neutron momentum density distribution of the reaction ^{4}He(π^+,$pppn$) with all three protons above the 30 MeV kinetic energy is shown in Fig. 7 for each incident pion energy. It is apparent that the neutron was a spectator in many cases, but sometimes took part in the absorption process as reflected by the flat part of the distribution. For a comparison to the $3NA$ mode in ^{3}He one has to ensure that one neutron in ^{4}He acted as a spectator. This was accomplished to a good approximation by a cut of $p_n \leqslant 200$ MeV/c on the final state neutron momentum. It was applied to all further ^{4}He distributions shown in this paper (except Fig. 8). Further, in order to make the proton distributions from the two target nuclei equivalent, those from ^{4}He are shown in this paper in the c.m. system of the three final state protons; we refer to this henceforth as the ppp subframe.

B. Soft final state interaction

The soft final state interaction (SFSI) may cause pairs of final state nucleons to be strongly correlated with small relative momentum. Figure 8 shows the SFSI effect observed by LADS and compared to a Jost proton-neutron SFSI enhancement function [37–40]. However, due to the finite segmentation of the LADS detector such pairs often could not be distinguished, which caused the event to be rejected. Thus it was important to take SFSI into account, both to determine the lost yield and to reproduce the measured distributions better, and so the Jost enhancement functions were included in all the Monte Carlo event generators. As seen in Fig. 8 the agreement between the anticipated and observed effect is satisfactory. Although less pronounced, the effect of proton-proton SFSI is also visible in the LADS data. Again, the Jost parametrization describes it reasonably well, and was included in the event generators.

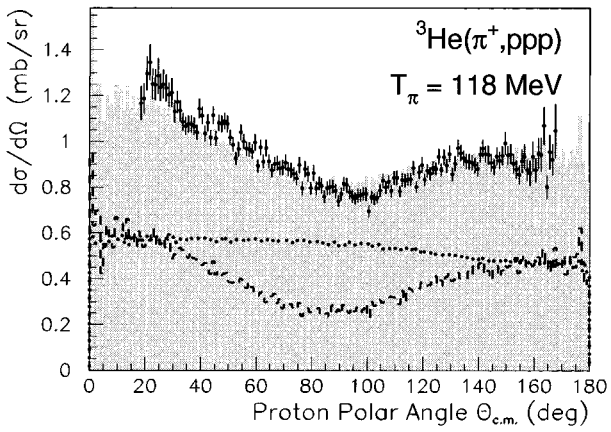

FIG. 9. Proton polar angle distribution with $T_p > 30$ MeV in the ppp subframe following the absorption of 118 MeV pions by ^{3}He. The dots with error bars are the efficiency corrected data, the lines are the fitted $2NA_{(pp)p}$ (dashed) and $3NA^{L\geqslant 0}_{(ppp)}$ (dotted) simulations with the shaded area as the sum of these.

C. Differential cross sections

1. Polar angle Θ_p

One of the simplest variables to investigate is the polar angle Θ_p of the protons in the ppp subframe. The distribution over this angle is presented in Fig. 9 for ^{3}He at an incident pion energy of 118 MeV. Each event is represented three times in this plot because of the proton multiplicity.

The spectrum is fairly flat but with a minimum near 90°, reminiscent of the $2NA$ distribution. Thus this distribution may be described quite well by a simple mixture of the flat $3NA^{L\geqslant 0}_{(ppp)}$ phase space and the $2NA_{(pp)p}$ distributions. As a result of comparisons over such simple kinematic variables as this angle or the recoil momentum it might be concluded, as was often the case with earlier experiments, that simple $3N$ phase space with a $2NA$ admixture from the tail of the spectator momentum distribution is sufficient to describe the three-proton final state. However, we show in this paper that the examination of other variables and their correlations demonstrates that such a picture is too simple.

2. Proton-proton opening angle ψ_{pp}

It was demonstrated in one of our previous works [15] that in ^{3}He ISI constitutes a significant fraction of the $3NA$ cross section. The proton-proton opening angle in the laboratory frame is useful for demonstrating and determining the importance of both ISI and HFSI.

If the three fast protons result from an initial state interaction followed by the quasifree $2N$ absorption process (ISI),

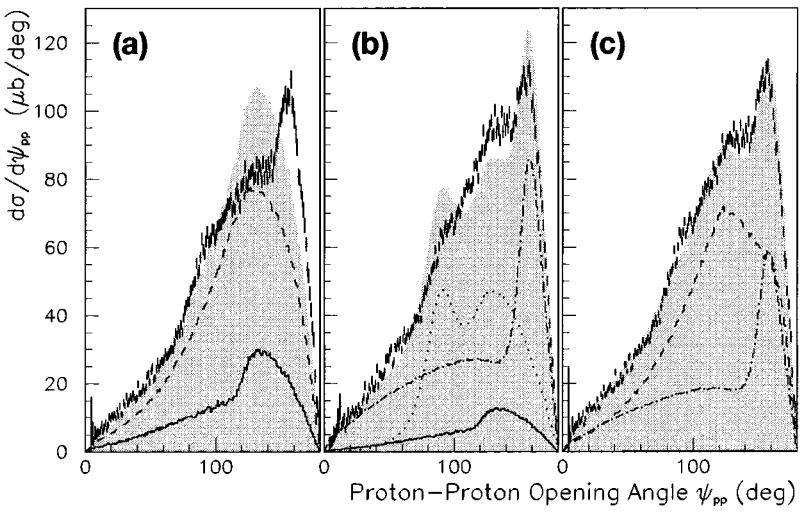

FIG. 10. Proton-proton opening angle ψ_{pp} in the laboratory frame for the reaction ^{3}He (π^+,ppp) with $T_p > 30$ MeV at $T_\pi = 239$ MeV. The data were fitted with different combinations of $2NA_{(pp)p}$ (solid line), $3NA_{(ppp)}$ (dashed), $\mathrm{ISI}_{(ppp)}$ (dash-dotted), and $\mathrm{HFSI}_{(ppp)}$ (dotted), as described in the text. The shaded areas are always the sums of the fitted simulations. The slightly different shapes of the data are due to changes in the acceptance correction when different models are used.

one proton pair should be almost back-to-back giving a peak in the opening angle distribution near 180°. On the other hand, if the three fast protons stem from a $2NA$ process followed by a nucleon-nucleon rescattering (HFSI), one proton pair should have an opening angle around 90° because of the identical masses of the two scattered protons.

To get an impression of the importance of these two-step processes, fits to the distributions of the data over the five independent variables (β, γ, ξ, $\psi_{\min}$, $\psi_{\max}$) were performed using three sets of models for the reaction $^3\mathrm{He}(\pi^+,ppp)$ at $T_\pi = 239$ MeV. For each set the five distributions were fitted simultaneously, with the strengths of the reaction models as the only free parameters.

The first set of models was composed of $2NA_{(pp)p}$ and $3NA^{L\geq 0}_{(ppp)}$ only, and the result of the fit is shown in Fig. 10(a). Though these models gave a reasonable description of the polar angle distribution at 118 MeV (Fig. 9), they clearly fail to reproduce the peak in the data around 160° at 239 MeV. A χ^2/DOF of 10.2 (DOF: degree of freedom) was obtained.

The second set was made up of $2NA_{(pp)p}$, $\mathrm{ISI}_{(ppp)}$, and $\mathrm{HFSI}_{(ppp)}$, and the result of the fit is shown in Fig. 10(b). As expected, the peak around 160° is reproduced only by the ISI model. However a peak at 90°, as suggested by the HFSI model, is hardly visible in the data. Though the χ^2/DOF improves to 7.7, these cascade mechanisms and $2NA$ alone are not able to provide a good description of the data.

The final set contained all five simulations discussed here and the fit result is shown in Fig. 10(c). The data distribution is now reasonably described by the models (χ^2/DOF=2.1). The ISI peak around 160° is reproduced well and the HFSI contribution vanishes, but the dominant contribution is phase space distributed $3NA$. This indicates that a significant amount of the multinucleon absorption strength in ^{3}He cannot be explained in a semiclassical cascade picture.

3. Azimuthal angle β

The independent variable β reflects the azimuthal rotation of the ppp c.m. plane around the beam axis. Since no direction other than the beam direction was specified in this experiment, there should be no dependence on this angle. Figure 11 shows that the data, corrected for the acceptance determined by the simulations, are indeed independent of β.

4. Plane angle ξ and angular momentum dependence

All former pion absorption experiments on ^{3}He and ^{4}He were largely limited to measurements in a plane containing the beam (in-plane). LADS is the first experiment which has the ability to investigate fully the phase space outside this plane (out-of-plane). The angle ξ describes the degree to which the event was out of plane.

As has been pointed out by Šimičević and Mateos [28], the distribution of the plane angle ξ is sensitive to the relative angular momentum l_π between the incident pion and the absorbing $3N$ system or, in other words, to the angular momentum L of the three-nucleon final state. Under the assumption of $3NA$ being a one-step process, the differential cross section taking into account angular momenta of up to L can then be parametrized by an expansion into Legendre polynomials similar to the quasideuteron absorption model:

$$\frac{d^2\sigma}{d\beta d\cos\xi} = \frac{d\sigma}{d\Omega_\xi} = \sum_{n=0}^{L} A_{2n} P_{2n}(\cos\xi). \qquad (5.1)$$

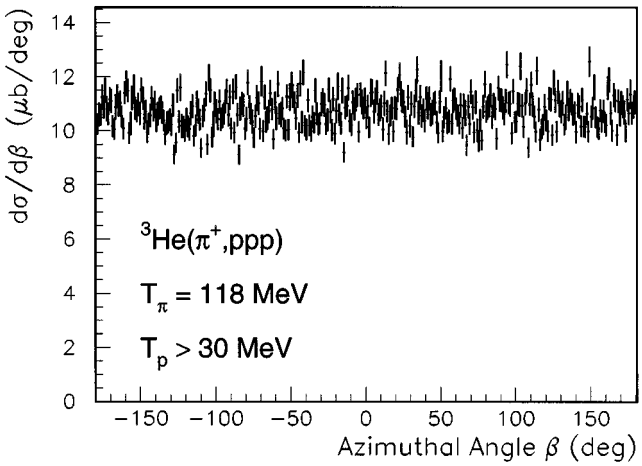

FIG. 11. Distribution of the azimuthal angle β for the reaction $^3\mathrm{He}(\pi^+,ppp)$ at $T_\pi = 118$ MeV.

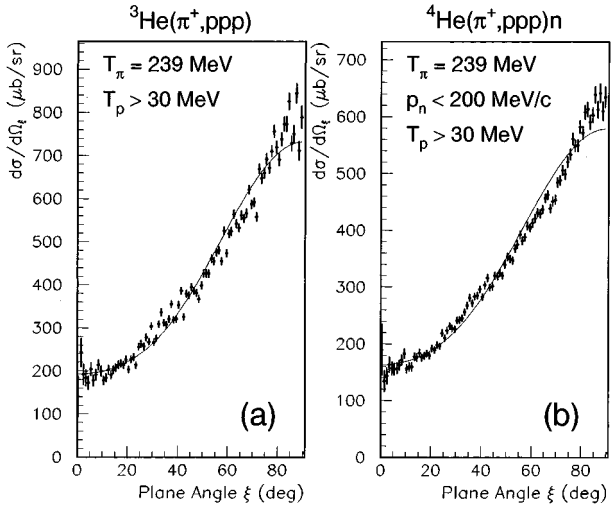

FIG. 12. Plane angle distribution of the (ppp) (a) and $(ppp)n$ (b) channel after absorption by ^{3}He and ^{4}He, respectively, for 239 MeV incident pion energy. The dots with error bars are the efficiency corrected data, the solid lines show a fit of the Legendre expansion Eq. (5.1).

If the $3NA$ mode were distributed like a simple phase space with $L=0$, the cross section $d\sigma/d\Omega_\xi$ would be a constant. On the other hand, deviations from a constant density in ξ show that contributions from nonzero angular momentum components are significant. The amount of the $L>0$ contribution should be related to the relative strengths of different reaction mechanisms.

The data are shown in Fig. 12. As can be immediately seen the distributions are far from being constant. That has two important consequences: First, the $3NA$ mode is not distributed according to simple phase space as assumed in most previous work; and second, a purely in-plane ($\xi=90°$) measurement of the $3NA$ reaction leads to an incorrect integrated cross section, if it is assumed that the distribution is constant over ξ.

The solid lines in Fig. 12 are fits of the Legendre expansion Eq. (5.1). These fits indicate that angular momenta of at least $L=2$ are necessary to describe the data well. The Legendre coefficients A_0, A_2, and A_4 obtained from the fits are summarized in Table II.

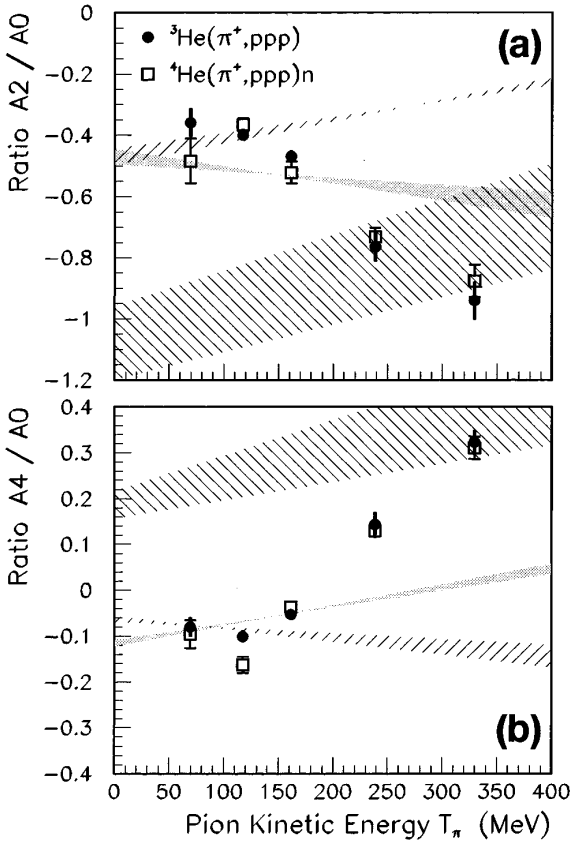

FIG. 13. Ratios $A2/A0$ (a) and $A4/A0$ (b) of the Legendre expansion Eq. (5.1) of the plane angle ξ as obtained from fits to the ppp data ($T_p>$ 30 MeV; $p_n<$ 200 MeV/c for ^{4}He) for the nuclei ^{3}He and ^{4}He. The error bars include the fit and normalization uncertainties. The bands reflect the predicted energy dependences from our semiclassical cascade models: $2NA$ (shaded), (ISI+$2NA$) [left-hatched, e.g., bottom of (a)], and ($2NA$+HFSI) (right-hatched).

TABLE II. $3NA$ Legendre coefficients [Eq. (5.1)] for the reactions ^{3}He(π^+,ppp) and ^{4}He (π^+,ppp)n, reflecting angular momentum components up to $L=2$. The first error bars of the coefficients are the fit errors, the second error bars of $A0$ reflect the normalization uncertainties. The uncertainties for the coefficient ratios contain both error sources.

Nucleus	T_π (MeV)	$A_0\left(\frac{\mu b}{sr}\right)$	$A_2\left(\frac{\mu b}{sr}\right)$	$A_4\left(\frac{\mu b}{sr}\right)$	$\frac{A_2}{A_0}$	$\frac{A_4}{A_0}$
	70	230±2±24	-82±3	-18±4	-0.36±0.04	-0.08±0.02
	118	606±3±18	-242±6	-61±6	-0.40±0.02	-0.10±0.01
^{3}He	162	884±4±24	-414±7	-47±7	-0.47±0.02	-0.05±0.01
	239	506±3±20	-387±5	72±5	-0.76±0.05	0.14±0.03
	330	198±2±10	-186±3	64±3	-0.94±0.06	0.32±0.03
	70	81±1±10	-39±2	-8±2	-0.48±0.07	-0.10±0.03
	118	240±2±8	-88±4	-39±4	-0.37±0.02	-0.16±0.02
^{4}He	162	485±3±29	-253±5	-18±5	-0.52±0.04	-0.04±0.01
	239	409±2±13	-299±5	53±5	-0.73±0.03	0.13±0.01
	330	289±3±14	-253±5	90±5	-0.88±0.05	0.31±0.02

The ratios A_2/A_0 and A_4/A_0 are plotted in Figs. 13(a) and 13(b), respectively, against the incident pion energy. The energy dependencies of the ratios have opposite slopes, but are the same for ^{3}He and ^{4}He within the uncertainties. In both nuclei higher angular momentum components become more important as the pion energy increases. These ratios may be compared to those describing the results of our simulations, which are also shown as shaded areas in Fig. 13. At lower pion energies the data show ratios similar to those of the $2NA$ and HFSI models, while at higher energies they are closer to the ISI models.

The fact that a second- and even higher order terms of a Legendre polynomial are necessary to describe the distribution of the plane angle ξ shows that there is a contribution from $l_\pi \geq 1$ coupling of the pion to the $3N$ system. Since the strongest interaction vertex in this energy region is the p wave $\pi N \rightarrow \Delta$, this result could indicate that this vertex is the initial coupling of the pion in the $3NA$ mode. This characteristic is present in both cascade processes (ISI+$2NA$) and ($2NA$+HFSI). Of course, this argument does not exclude other $3NA$ mechanisms, but if one also takes into account the energy dependence of the $3NA$ mode (see Fig. 22), a coupling to the Δ appears likely in any case.

The Legendre coefficients can also be used to quantitatively compare the $3NA$ cross sections to those from previous in-plane experiments, where a constant s-wave matrix element was assumed for extrapolation over unmeasured phase space. From our parametrization of the ξ distribution we calculate that using this assumption leads to an overestimate of the amount of $3NA$ by 15%, 16%, 21%, 44%, and 59% for ^{3}He, and 20%, 12%, 25%, 41%, and 55% for ^{4}He, at pion energies of 70, 118, 162, 239, and 330 MeV, respectively. Some of the previously reported results on ^{3}He [2–5,8] may have reflected such overestimates, but there is not very good agreement between them on the magnitude of the $3NA$ cross section. Nevertheless, the general physics conclusion drawn in these papers, that there is a significant amount of $3NA$, is not changed by such errors. We are convinced that the present results are considerably more reliable because of the large solid angle coverage and the small systematic uncertainties.

Besides the physics information that can be gained from the plane angle ξ it is an important variable for the full description of the $3N$ channel and its decomposition into mechanisms. The ξ data on ^{3}He for all five incident pion energies are shown in Fig. 14 and compared to those of ^{4}He. The distributions are similar for both nuclei and reasonably well reproduced by the fits of the simulations.

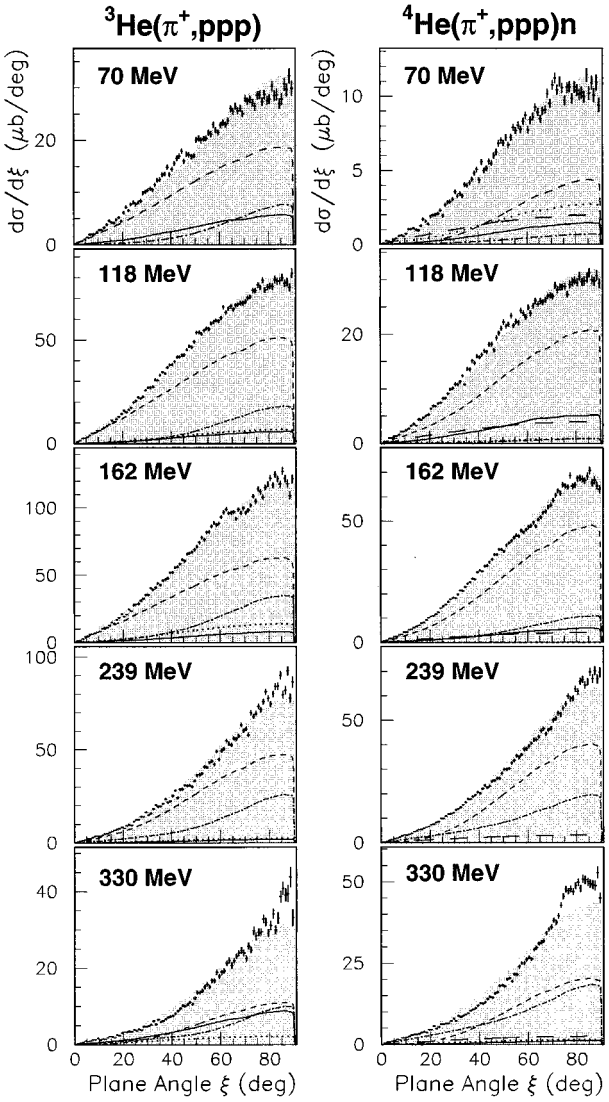

FIG. 14. Plane angle ξ distributions of the ^{3}He(π^+,ppp) (left column) and ^{4}He(π^+,ppp)n (right column) reactions for $T_\pi = 70$, 118, 162, 239, and 330 MeV. All spectra are acceptance corrected with a threshold of $T_p = 30$ MeV. The dots with the error bars are the data and the shaded areas the sums of the simulations. The lines are the fitted contributions of the simulations for $2NA$ (solid), summed $3N$ phase space for $L \geq 0$ and $L \geq 1$ (short-dashed), ISI (dash-dotted), and HFSI (dotted). The long-dashed lines of the ^{4}He fits are the sums of the tails of the $4NA_{(pppn)}$ and $3NA_{(ppn)p}$ simulations.

5. *Rotation angle γ and its sensitivity to reaction mechanisms*

The rotation angle γ turned out to be the most sensitive of the independent variables in distinguishing between reaction mechanisms. With zero energy threshold, events uniformly filling $3N$ and $4N$ phase space give a constant distribution in γ, independent of the incident pion's angular momentum, while all other simulated absorption mechanisms show structures. This is illustrated in Fig. 15(a) for the reaction ^{3}He(π^+,ppp). As can be seen, the $2NA$ mode is strongly enhanced around $|\gamma| = 180°$, while the cascade mechanism ISI peaks around $|\gamma| = 0°$. HFSI lies somewhere in between and is strongly asymmetric.

The detector acceptance changes these distributions considerably. As can be seen from Fig. 15(b), a 30 MeV threshold cuts most strongly around $|\gamma| = 180°$. The distributions of $3N$ phase space events increase smoothly from $\gamma = -180°$ to $\gamma = 0°$ and fall off at positive angles almost symmetrically. As expected, most of the $2NA$ events are cut off, but the distribution should still be distinguishable from the $3N$ phase space and ISI mechanisms. Only HFSI is no longer very well separated. The least affected mechanism

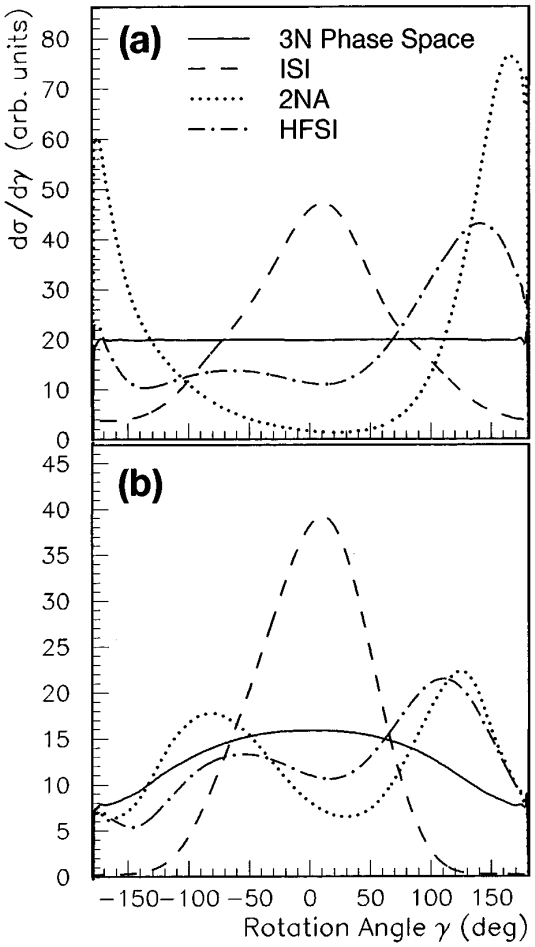

FIG. 15. Comparison of the rotation angle distributions of the ppp final state from ^{3}He at $T_\pi = 162$ MeV for the different simulations used in the analysis with $T_p > 0$ MeV (a) and with $T_p > 30$ MeV (b).

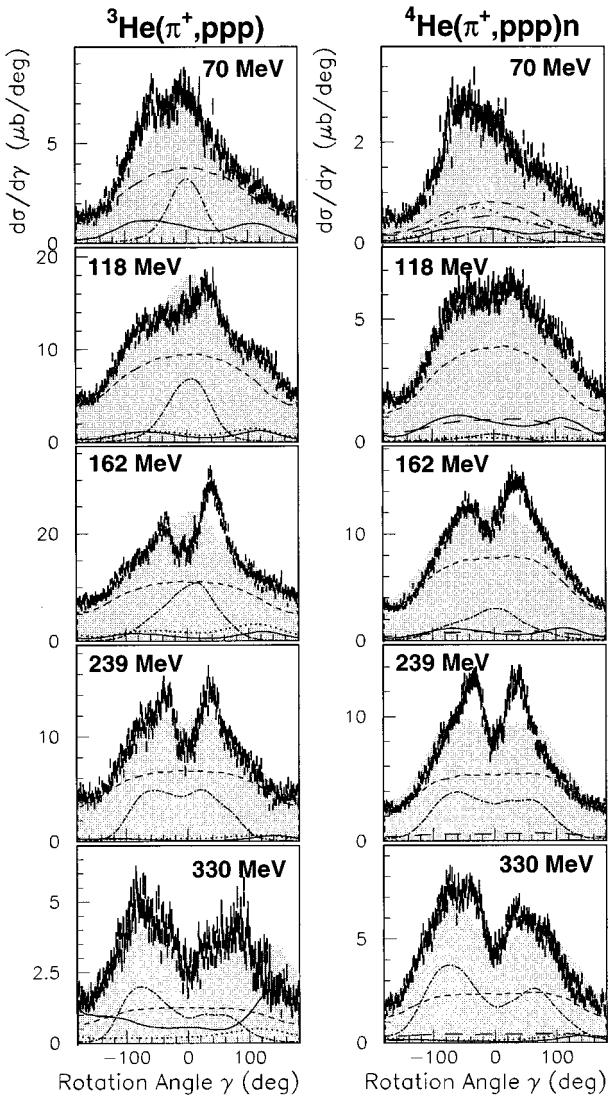

FIG. 16. Rotation angle γ distributions of the ^{3}He(π^+,ppp) (left column) and ^{4}He(π^+,ppp)n (right column) reactions for $T_\pi = 70$, 118, 162, 239, and 330 MeV. All spectra are acceptance corrected with a threshold of $T_p = 30$ MeV. The dots with the error bars are the data and the shaded areas the sums of the simulations. The lines are the fitted contributions of the simulations for $2NA$ (solid), summed $3N$ phase space for $L \geqslant 0$ and $L \geqslant 1$ (short-dashed), ISI (dash-dotted), and HFSI (dotted). The long-dashed lines of the ^{4}He fits are the sums of the tails of the $4NA_{(pppn)}$ and $3NA_{(ppn)p}$ simulations.

seems to be ISI which retains its clear signature around $|\gamma| = 0°$.

The acceptance corrected γ distributions are shown in Fig. 16 for events with $T_p > 30$ MeV. In all spectra there are clear deviations from the distributions for $3N$ phase space. Since γ is independent of ξ, these deviations cannot be explained by the observed angular momentum dependence, but must have a different origin. The structures become more pronounced as the incident pion energy increases, indicating that using only a phase space model for $3NA$ then becomes even less justified.

The only models coming close to a satisfactory description of the structures of the data are cascade ISI and phase space $3NA$. Only a combination of these can produce a strong enhancement in yield in the central part of the γ distributions, broadly similar to that in the data. From the distributions for $2NA$ and HFSI one can also conclude that a lot of the observed strength cannot be explained by these mechanisms, since both give a smooth minimum around $|\gamma| = 0°$ and peak in regions where the cross section is small. Nevertheless, the detailed structures in the data around 0° are not well reproduced by the simulations, and possible implications of this will be discussed below.

We note here again the similarity of the distributions in both nuclei. Although γ is rather sensitive to thresholds and mechanisms, both ^{3}He and ^{4}He show almost the same structures at each energy.

6. Minimum opening angle $\psi_{\min}$ and maximum opening angle $\psi_{\max}$

In Fig. 17 and Fig. 18 the spectra of the minimum and maximum opening angles $\psi_{\min}$ and $\psi_{\max}$, respectively, are compared for ^{3}He and ^{4}He at the different incident pion energies. No distinguishing structures exist in these variables and the data are reasonably well reproduced by the fits. The

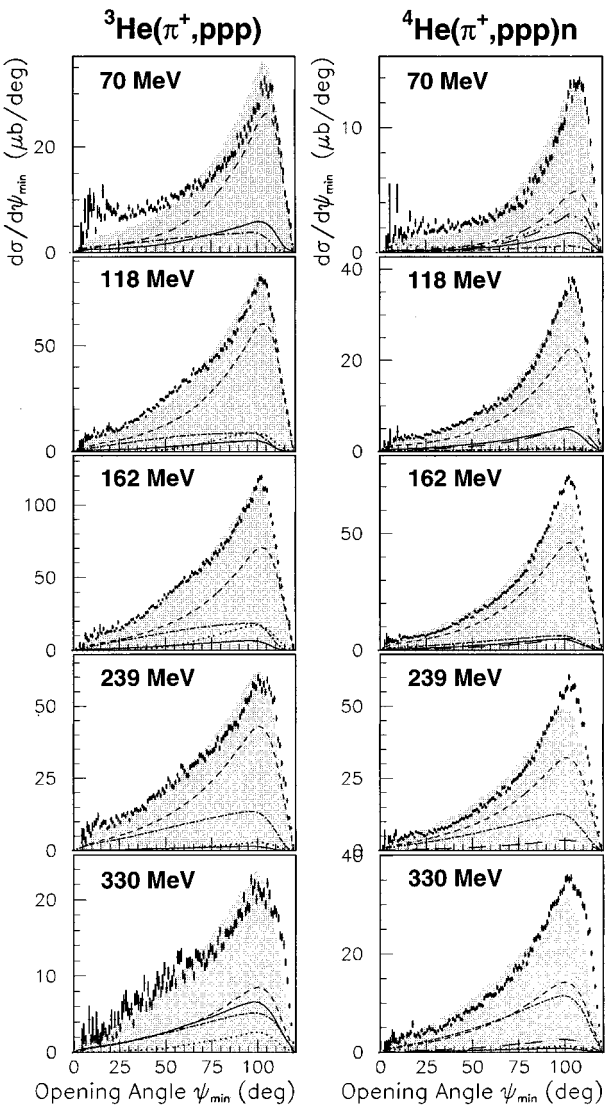

FIG. 17. Minimum opening angle $\psi_{\min}$ distributions of the ^{3}He(π^+,ppp) (left column) and ^{4}He(π^+,ppp)n (right column) reactions for $T_\pi = 70$, 118, 162, 239, and 330 MeV. All spectra are acceptance corrected with a threshold of $T_p = 30$ MeV. The dots with the error bars are the data and the shaded areas the sums of the simulations. The lines are the fitted contributions of the simulations for $2NA$ (solid), summed $3N$ phase space for $L \geqslant 0$ and $L \geqslant 1$ (short-dashed), ISI (dash-dotted), and HFSI (dotted). The long-dashed lines of the ^{4}He fits are the sums of the tails of the $4NA_{(pppn)}$ and $3NA_{(ppn)p}$ simulations.

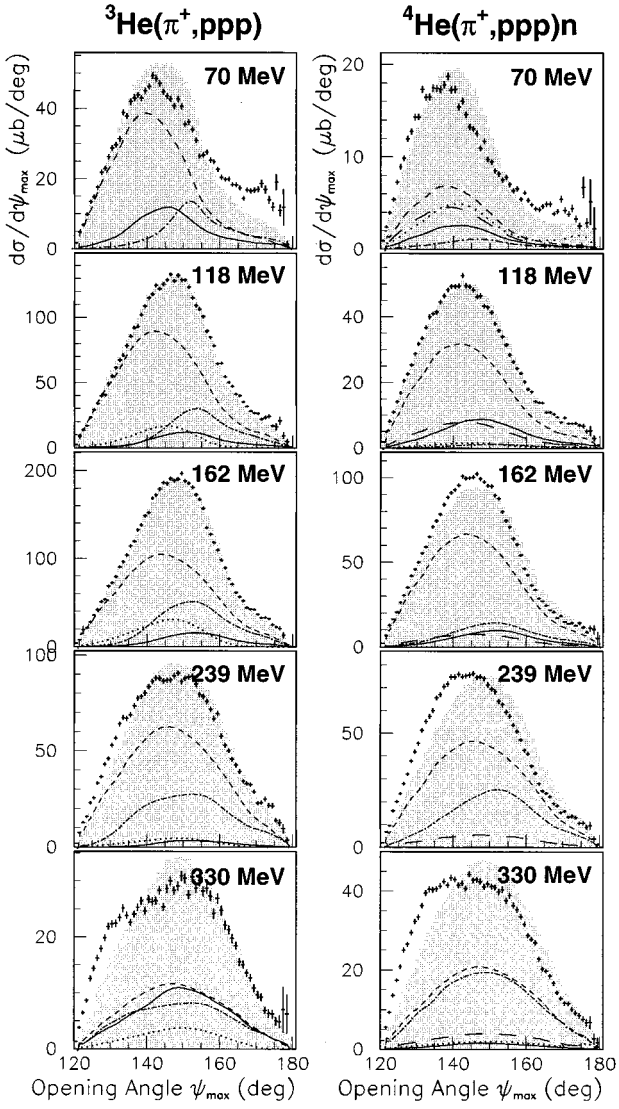

FIG. 18. Maximum opening angle $\psi_{\max}$ distributions of the ^{3}He(π^+,ppp) (left column) and ^{4}He(π^+,ppp)n (right column) reactions for $T_\pi = 70$, 118, 162, 239, and 330 MeV. All spectra are acceptance corrected with a threshold of $T_p = 30$ MeV. The dots with the error bars are the data and the shaded areas the sums of the simulations. The lines are the fitted contributions of the simulations for $2NA$ (solid), summed $3N$ phase space for $L \geqslant 0$ and $L \geqslant 1$ (short-dashed), ISI (dash-dotted), and HFSI (dotted). The long-dashed lines of the ^{4}He fits are the sums of the tails of the $4NA_{(pppn)}$ and $3NA_{(ppn)p}$ simulations.

fact that there is strength almost down to $\psi_{\min} = 0°$ is a reflection of the proton-proton soft final state interaction. Again, the distributions are very similar for both nuclei.

7. Dalitz plots

As already mentioned above, the triangular Dalitz plot is characterized by a constant event density in phase space. Therefore, any deviation from uniformity is a reflection of a nonconstant matrix element. For $3NA$ this means that any structures in this Dalitz plot (except in the threshold regions) are evidence for processes with more distinct kinematic features than phase space. If the absorption process is $2NA$, then the third nucleon is a spectator and is almost at rest, while the other two are about equal in kinetic energy and emerge back-to-back. These events populate the boundary region around $x = 0$ MeV and minimum y (see Fig. 3) and the two other symmetrically equivalent regions. Events with strongly correlated ejectiles, resulting from SFSI, are characterized by two particles with similar momenta with the third one in the opposite direction. Such final states are found in the boundary region at $x = 0$ MeV and maximum y. Both ISI and HFSI processes produce structures in the Dalitz plots, whose locations are dependent upon the incident pion energy. As examples, we show the results for our ISI and HFSI simulations for ^{3}He at 162 MeV in Fig. 19. The central

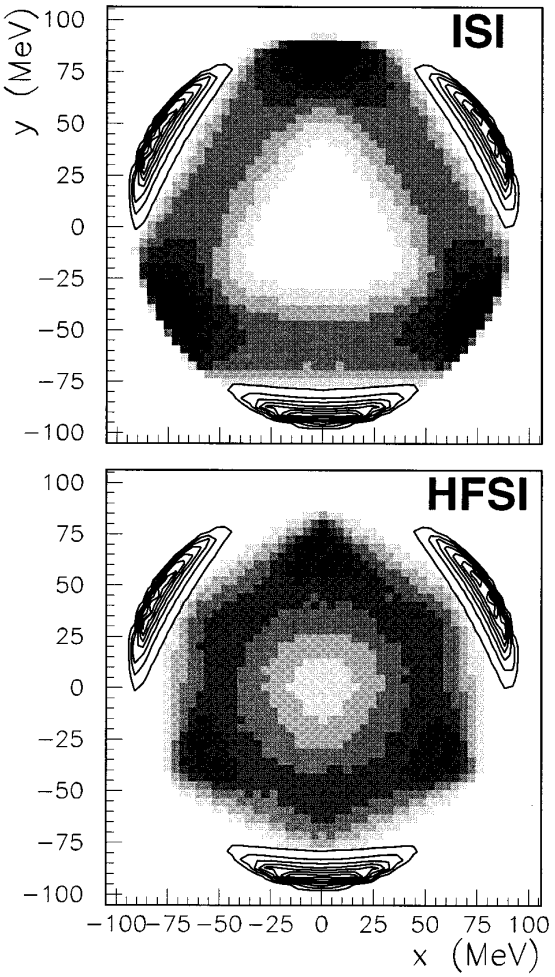

FIG. 19. Triangular Dalitz plot of a simulation of the ISI (upper) and the HFSI (lower) process for π^+ absorption on ^{3}He at 162 MeV. All protons were above a threshold of 30 MeV. The two plots have the same normalizations with the same number of events generated. For comparison the location of a simulation of the $2NA$ strength with no proton energy threshold applied (contour lines) is also shown in both plots.

region of the Dalitz plots ($x=0$ MeV and $y=0$ MeV), where all three particles have about the same kinetic energy, is mainly filled by the $3NA$ phase space simulations.

The advantage of this work in studying Dalitz plots is the full solid angle coverage of LADS and therefore the simultaneous measurement of all kinematic regions. In Figs. 20 and 21 the Dalitz plots for the reactions ^{3}He(π^+,ppp) and ^{4}He$(\pi^+,ppp)n$, respectively, are shown for the five measured pion energies and compared to the sum of the fitted simulations. The threshold of 30 MeV kinetic energy for all protons cuts off the $2NA$ regions in all plots.

Both in the data and in the simulation plots we find deviations from a constant event density. However, for both nuclei and all five energies the boundary regions of the Dalitz plot data are reproduced by the fitted simulations. This indicates that the contributions of SFSI, HFSI, and ISI to the $3NA(ppp)$ yield are reasonably well understood. This is not the case for the Dalitz plot interior: in particular the ^{4}He data (Fig. 21) show significant deviations from the model predictions in these regions. The degree of disagreement between data and simulations seems to increase with the pion energy. It should be noted that these structures are correlated to the unexplained features in the distributions of the rotation angle γ. Various semiclassical multistep models, e.g., involving $\Delta-N$ dynamics, were tested to account for these bumps, but no explanation was found.

It is also interesting to note that these unexplained structures exist in the ^{3}He data (Fig. 20) as well, but to considerably lesser extent. Our semiclassical models do not explicitly take into account the different nucleon densities and wave functions of ^{3}He and ^{4}He. Therefore, effects that may depend strongly on these quantities, such as interferences between partial waves of elementary processes, are not accounted for in our simulations. If a coherent $3NA$ process did indeed exist, one should also expect some interference between the partial waves of this process and of $2NA$. The increasing importance of the unexplained structures with the incident pion energy and their different strengths for ^{3}He and ^{4}He could also suggest such an effect, since we know that the relative multinucleon absorption yield as compared to the total absorption cross section shows a similar tendency.

D. Integrated cross sections and fractional decomposition into mechanisms

1. Cross sections

(a) ^{3}He: The total and the $2NA$ and $3NA$ partial cross sections for absorption on ^{3}He are given in Table III. The $3NA$ partial cross sections were obtained from the distributions discussed in the previous section, using the fitted Monte Carlo distributions to correct for the detector acceptance and to extrapolate over unmeasured kinematic regions, in particular down to very low proton energy. The fits provided in addition the separation of the $3NA$ from the $2NA$ yields. Also given in Table III are the total yields of three protons above 20 and 30 MeV; these yields are less model dependent, not requiring the extrapolation to low energy, and also have no subtraction of the $2NA$ component.

For the three central energies, the total absorption cross sections given in Table III are taken from Ref. [7], which reported the results of an earlier analysis of these data which was carried out in a way designed to minimize the uncertainty on this quantity. In contrast, the analysis reported here provides a more detailed identification of the $3NA$ yield than that of Ref. [7]. Thus, the $2NA$ partial cross sections given in Table III for these three energies are the differences between the total cross sections from Ref. [7] and the $3NA$ cross sections of the current analysis.

At 70 and 330 MeV the total absorption cross sections given in Table III were obtained as follows. For all events it was required that at least two protons be fully measured; if the third proton was not measured it was reconstructed (with kinematic redundancy) from the two measured ones. If all three protons were measured, the momentum of the lowest energy proton was taken to be that given by a similar reconstruction of its kinematics from the other two protons, rather than the measured value; this provided a more internally consistent set of data. Then this full data set was fitted with the procedures described in this paper, and the result provided

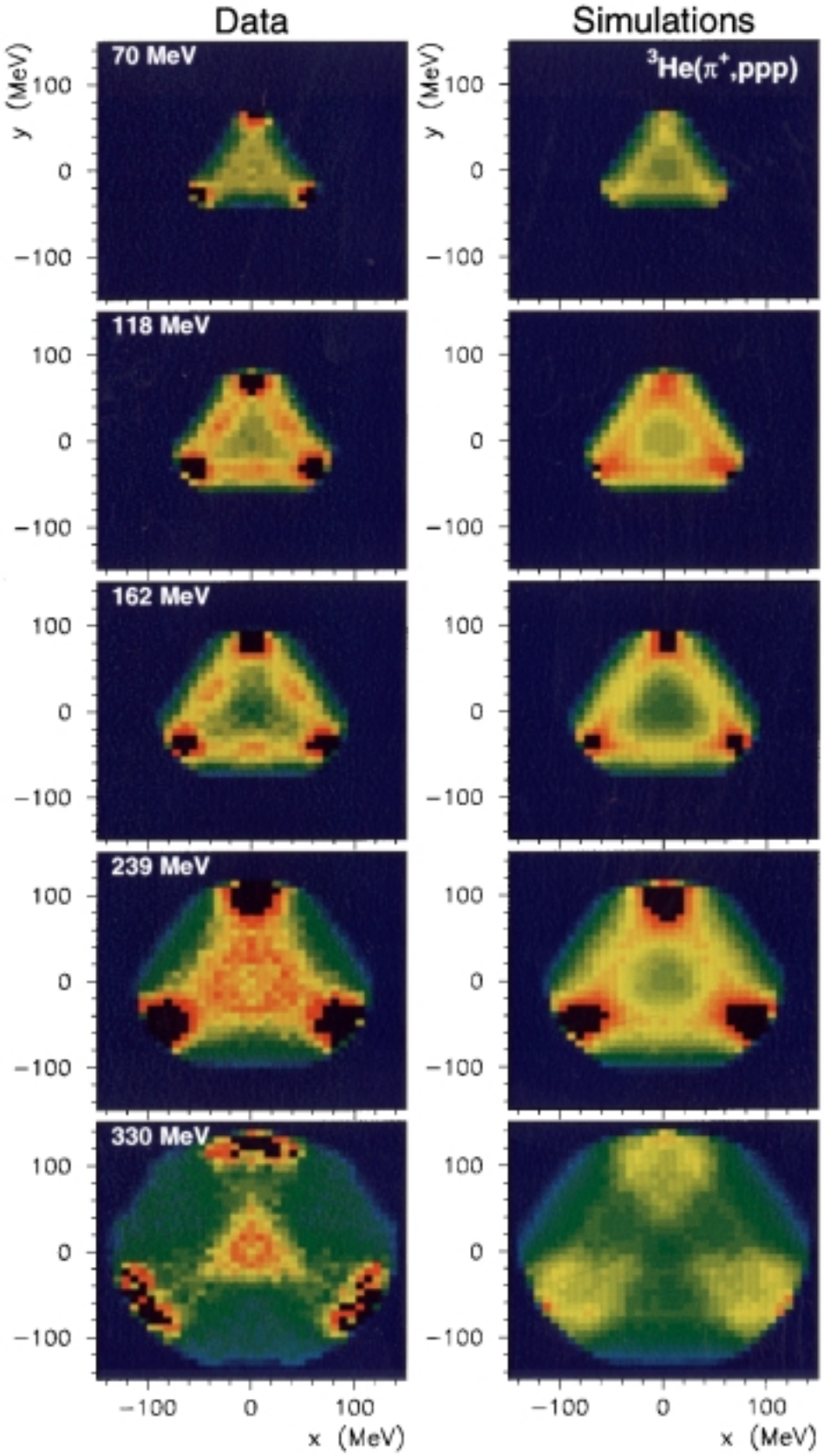

FIG. 20. (Color). Triangular Dalitz plots for the reaction ^{3}He(π^+,ppp) at T_π=70, 118, 162, 239, and 330 MeV with T_p>30 MeV. Left column, acceptance corrected data; right column, sum of simulations normalized to the data according to the fractional decomposition of Table V. For each energy the plots of the data and the simulations are normalized to the same maximum value in the z direction. The color sequence blue, green, yellow, brown, black indicates the increasing yield. Each change in color corresponds to an equidistant change in the linear z scale.

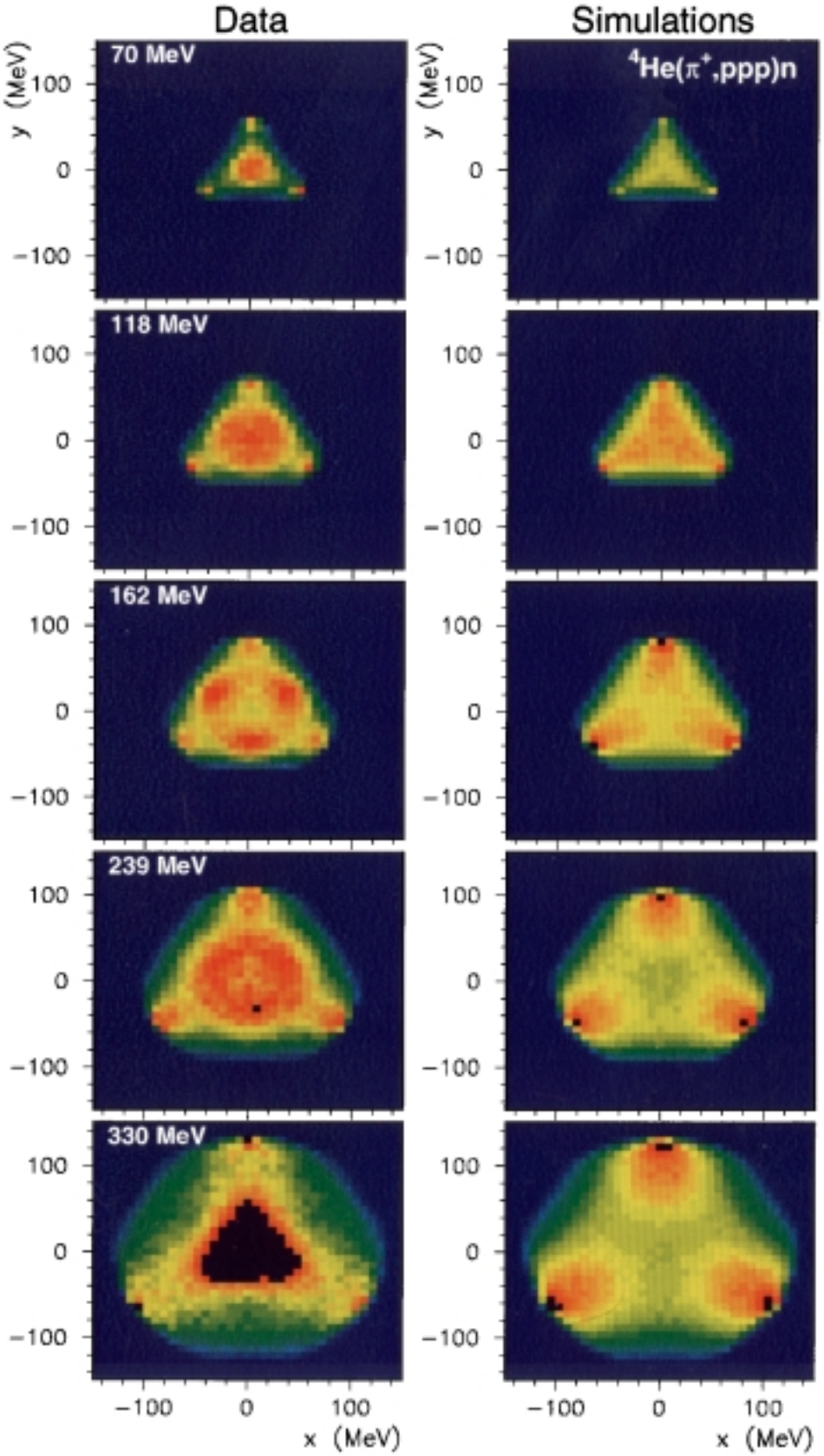

FIG. 21. (Color). Triangular Dalitz plots for the reaction ^{4}He(π^+,ppp)n at $T_\pi = 70$, 118, 162, 239, and 330 MeV with $T_p > 30$ MeV and $p_n < 200$ MeV/c. Left column, acceptance corrected data; right column, sum of simulations normalized to the data according to the fractional decomposition of Table V. For each energy the plots of the data and the simulations are normalized to the same maximum value in the z direction. The color sequence blue, green, yellow, brown, black indicates the increasing yield. Each change in color corresponds to an equidistant change in the linear z scale.

TABLE III. Total absorption and partial $2NA$ and $3NA$ cross sections for positive pion absorption on ^{3}He (σ_{abs} for 118, 162, and 239 MeV are from Ref. [7]). The total $3p$ yield is also given for different thresholds. For $3NA$ and the $3p$ yields the first error is due to different models and fits, and the second error reflects the normalization uncertainties.

	Total	$2NA$	$3NA$	$3p$ yield	
T_π (MeV)	σ_{abs} (mb)	$\sigma_{(pp)p}$ (mb)	$\sigma_{(ppp)}$ (mb)	$\sigma_{(ppp)}^{T_p>20\text{ MeV}}$ (mb)	$\sigma_{(ppp)}^{T_p>30\text{MeV}}$ (mb)
70	19.4±2.1	16.6±2.2	2.8±0.6±0.3	2.59±0.04±0.27	1.50±0.03±0.16
118	27.3±0.8	21.0±1.1	6.3±0.7±0.2	5.80±0.06±0.17	3.87±0.04±0.11
162	24.7±0.7	17.1±0.8	7.6±0.5±0.2	7.25±0.08±0.21	5.56±0.08±0.16
239	10.0±0.4	6.2±0.5	3.8±0.2±0.2	3.61±0.03±0.14	3.12±0.03±0.12
330	3.1±0.3	1.9±0.4	1.2±0.2±0.1	1.26±0.02±0.06	1.18±0.01±0.06

the total absorption cross sections at these two energies. The $2NA$ partial cross sections were again obtained by subtraction of the $3NA$ from the total cross section. Total cross sections obtained by this procedure for the three central energies were consistent with those from Ref. [7].

The two errors given for the $3NA$ cross sections in Tables III and IV reflect the separate uncertainties due to the various models and choices of distributions used for the fits and to the beam normalization, respectively. The uncertainties given for the total cross sections combine both errors. The $2NA$ uncertainty is gained from the quadratic sum of the error on the total and on the $3NA$ yield.

The energy dependence of the $3NA$ cross section $\sigma_{(ppp)}$ peaks at a higher energy than the ^{2}H absorption cross section (Fig. 22), but shows a similar shape. This strongly suggests that Δ excitations also play a significant role in $3N$ absorption.

Compared to previous measurements [2–5] the total absorption and the $2NA$ cross sections of this work are somewhat higher at 70 and 118 MeV, while they agree well for pion energies of 162 MeV and higher. This result causes a shift in the peak energy and brings the observations on ^{3}He into better agreement with those on other light nuclei [25,31]. Our $3NA$ cross sections appear a bit higher than those of Ref. [4], but about match the data of Refs. [2,3,5]. The lesser systematic uncertainties in the cross sections of this work make us believe that these are more reliable.

(b) ^{4}He: Because absorption on ^{4}He often leads to a $pppn$ final state, the total and $2NA$ cross sections for this nucleus cannot be determined with the procedure described in this paper. How to determine these quantities is described in detail in Ref. [25]. We will restrict ourselves here to the presentation of the $3NA$ partial cross sections $\sigma_{(ppp)n}$, which are given in Table IV. Our data points are higher than a previous measurement at 118 MeV [9], but in agreement with another one at 165 MeV [10].

It is striking that the $3NA(ppp)$ cross section on ^{4}He is smaller than that on ^{3}He at the three lower pion energies, whereas simple counting of the number of nucleons would suggest that the ^{4}He cross section would always be higher. Although we again find a shape of the $3NA(ppp)$ yield (Fig. 22) that is very similar to a Δ excitation function, the peak position is shifted to higher energies than in ^{3}He. As already mentioned there are competing channels in ^{4}He that can remove strength from the $\sigma_{(ppp)n}$. For example, final state interactions may move parts of the yield to the (ppd) and $(pppn)$ channels. Because of cross section arguments these losses are expected to be larger at lower incident pion energies, which might explain the deficit in yield compared to ^{3}He in this energy region. Another reason could simply be the higher binding energy of ^{4}He, which reduces the available phase space especially at low energies.

It should be again noted here that the cross sections with thresholds ($T_p>20$ MeV or $T_p>30$ MeV and $p_n<200$ MeV/c), given in Table IV, are not corrected for tails of the other channels, $2NA$, $3NA(ppn)$, and $4NA$, while the zero threshold yields are.

2. Decomposition of 3NA into mechanisms

One of the main issues of this paper is to address the question of how much of the $3NA$ cross section can be un-

TABLE IV. $3NA$ cross sections for the reaction ^{4}He$(\pi^+,ppp)n$. The $3p$ yield is also given for different thresholds (in these cases the neutron momentum was required to be less than 200 MeV/c). The first error is due to different models and fits, the second error reflects the normalization uncertainties.

	$3NA$	$3p$ yield	
T_π (MeV)	$\sigma_{(ppp)n}$ (mb)	$\sigma_{(ppp)n}^{T_p>20\text{ MeV}}$ (mb)	$\sigma_{(ppp)n}^{T_p>30\text{ MeV}}$ (mb)
70	2.0±0.6±0.3	1.04±0.01±0.14	0.52±0.01±0.07
118	3.8±0.4±0.1	2.38±0.03±0.08	1.54±0.02±0.05
162	5.9±0.4±0.4	3.95±0.02±0.24	3.08±0.04±0.19
239	4.3±0.2±0.1	2.92±0.03±0.09	2.56±0.03±0.08
330	2.6±0.2±0.1	1.89±0.03±0.10	1.73±0.02±0.09

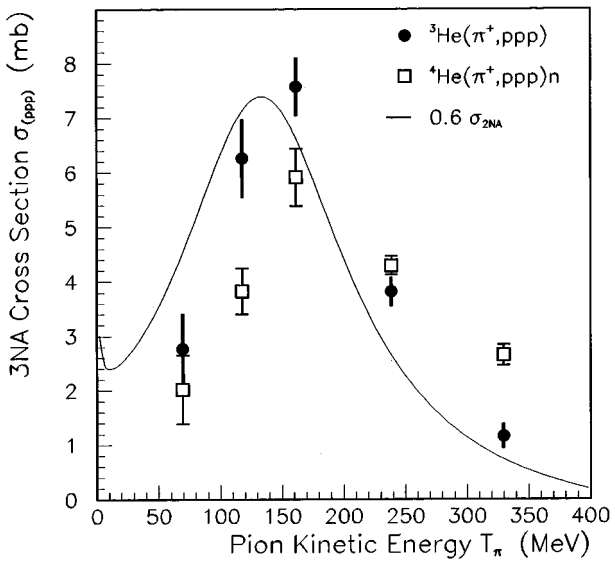

FIG. 22. $3NA(ppp)$ cross sections for ^{3}He and ^{4}He. The solid line is the parametrized deuterium absorption cross section [31] scaled by a factor of 0.60.

derstood in terms of cascade processes. It was shown in Ref. [15] that in the Δ-resonance region between 3% and 12% of the total pion absorption cross section of ^{3}He, or 13–33 % of the $3NA$ yield, can be attributed to an ISI process followed by $2NA$. Of course, these fractions are interesting also below and above the resonance region, and especially on the heavier ^{4}He nucleus.

Decompositions of the zero-threshold $3NA(ppp)$ reaction into cascadelike ISI and other processes, deduced from the fits to the data described in this paper, are given in Table V. As in Ref. [15] it was found that it was not possible to reliably deduce the relative strengths of HFSI and $3N$ phase space ($3N$-PS) from the fits, and so the individual contributions from these models are not given. The percentages given in Table V are average values of the results of fits to different variable sets and with various thresholds applied. The cited uncertainties are the standard deviations of the results from the fits of our models.

The fraction of the $3NA(ppp)$ yield attributable to the mechanism (ISI+$2NA$) appears to increase with pion energy for both ^{3}He and ^{4}He. This trend can be understood qualitatively by simple consideration of the free πN and $2NA$ cross sections. In ^{4}He particularly, the ISI is presumably suppressed at low energies due to binding energy effects: pions at low incident energy cannot easily transfer enough energy quasielastically to overcome the proton's binding.

Because of the absence of distinct signatures in the data, the attributed division between $3N$-PS($L \geqslant 0$), $3N$-PS ($L \geqslant 1$), and HFSI was very dependent on the conditions of the fit. However, the sum of the two phase space models alone was typically given as about two thirds of the $3NA$ (ppp) cross section (and almost always over half). In addition, the $3N$-PS($L \geqslant 1$) part tended to be favored over $3N$-PS($L \geqslant 0$) in ^{4}He at all pion energies and in ^{3}He above resonance.

Any HFSI yield indicated by the fits was usually smaller than the ISI yield, which might be a reflection of the NN cross section being weaker than that for πN. On the other hand, the kinematic signatures for HFSI appear to be less marked than for ISI, making the determination of its strength less secure.

It should be noted here that in all models the effect of SFSI is included. Though hard to quantify, the yield from this is stronger at low pion energies and, because of the proton-neutron SFSI, also in ^{4}He than in ^{3}He. However, it is small compared to the $3NA(ppp)$ cross sections.

VI. CONCLUSIONS

In this paper we have presented an analysis of the three-proton $3NA$ on ^{3}He and ^{4}He making use of a complete set of variables. Distributions and cross sections were determined for five incident pion energies over the Δ-resonance region.

We have shown that measurements in noncoplanar geometries are important for the investigation of multinucleon pion absorption. Hence the assumption made by previous experiments, that the $3NA$ mode is distributed like s-wave phase space, is too crude. P-wave components apparently are needed to describe the noncoplanar behavior of the data, consistent with an initial $\pi N \rightarrow \Delta$ coupling occurring in $3NA$. The importance of coupling to the Δ is also supported by the energy dependence of the $3NA(ppp)$ cross section for both nuclei.

Fits to the data suggest that a significant fraction of the $3NA(ppp)$ yield can be described by a semiclassical (ISI+$2NA$) cascade model. This fraction increases with the incident pion energy as would be expected with the Δ couplings

TABLE V. Fractional decomposition of the $3NA(ppp)$ cross section into absorption mechanisms at zero threshold for the reactions ^{3}He(π^+,ppp) and ^{4}He(π^+,ppp)n.

	^{3}He		^{4}He	
T_π (MeV)	(ISI+$2NA$)	($2NA$+HFSI) +$3N-$PS($L \geqslant 0$) +$3N-$PS($L \geqslant 1$)	(ISI+$2NA$)	($2NA$+HFSI) +$3N-$PS($L \geqslant 0$) +$3N-$PS($L \geqslant 1$)
70	26±7 %	74±7 %	11±8 %	89±8 %
118	17±3 %	83±3 %	4±3 %	96±3 %
162	21±2 %	79±2 %	16±5 %	84±5 %
239	26±2 %	74±2 %	29±9 %	71±9 %
330	28±5 %	72±5 %	38±13 %	62±13 %

in both steps. The data do not reveal distinct kinematic signatures as suggested for a similar ($2NA$+HFSI) cascade process; however, given that the NN cross section is significantly smaller than the πN one, this relative weakness may not be surprising.

Our investigations of the differential cross sections suggest that these ISI and HFSI cascade mechanisms, approximated by semiclassical models, can account for less than half of the total $3NA(ppp)$ yield in both ^{3}He and ^{4}He. We have approximated the remaining yield with $L \geq 0$ and $L \geq 1$ $3N$ phase space distributions. However, there are additional structures in the data, especially in the rotation angle distributions and the Dalitz plots, that are not reproduced by any of our models.

The $3NA(ppp)$ distributions in both nuclei are remarkably similar, even showing the same unexplained structures. The degree of similarity seems surprising since our cascade models suggest significant smearing of the distributions as a consequence of the different nuclear environment in ^{4}He. This indicates that the same mechanisms are responsible for the $3N$ absorption on ^{3}He and ^{4}He.

We were unable to find an explanation for the structures by varying the details of our models or considering other plausible multistep processes, e.g., involving $\Delta - N$ dynamics. However, none of these models permits the inclusion of interference between partial waves of different elementary processes, which could be the origin of some of these structures. In fact, very preliminary results of Faddeev-type calculations of the π-^{3}He absorption [44] suggest that such interferences may be important.

Finally, considering the overall results of the analysis presented here, the probability that a significant part of the $3NA$ cross section stems from a coherent $3N$ process involving dynamics not yet considered in this paper cannot be excluded. Indeed, the similarity of the ppp distributions observed for ^{3}He and ^{4}He and the difficulty in describing significant features of the data in the context of the models considered may point to such new dynamics. It is also striking that the relative size and energy dependence of the $3NA(ppp)$ cross section in ^{3}He and ^{4}He are not at all consistent with expectations from simple models which essentially depend on the numbers of target protons and neutrons. However, one expects that in ^{4}He the other channels, (ppn), (ppd), and $(pppn)$, will compete with the (ppp) $3NA$ channel. Therefore, a definitive explanation of the ratio of the ppp yield in the two nuclei must wait at least for a comparison of these competing channels. In this regard a quantitative comparison of the ^{4}He (ppp) and (ppn) channels should prove especially instructive in understanding the isospin structure of the $3NA$ process.

ACKNOWLEDGMENTS

We thank the technical staff of the Paul Scherrer Institute for the support provided to this experiment. We also thank H. Kamada and M. Locher for useful discussions. This work was supported in part by the German Bundesministerium für Forschung und Technologie (BMFT), the German Internationales Büro der Kernforschungsanlage Jülich, the Swiss National Science Foundation, the U.S. Department of Energy (DOE), and the U.S. National Science Foundation (NSF).

[1] G. Backenstoss, M. Izycki, P. Salvisberg, M. Steinacher, P. Weber, H. J. Weyer, S. Cierjacks, S. Ljungfelt, H. Ullrich, M. Furić, and T. Petković, Phys. Rev. Lett. **55**, 2782 (1985).

[2] K. A. Aniol, A. Altman, R. R. Johnson, H. W. Roser, R. Tacik, U. Wienands, D. Ashery, J. Alster, M. A. Moinester, E. Piasetzky, D. R. Gill, and J. Vincent, Phys. Rev. C **33**, 1714 (1986).

[3] L. C. Smith, R. C. Minehart, D. Ashery, E. Piasetsky, M. Moinester, I. Navon, D. F. Geesaman, J. P. Schiffer, G. Stephens, B. Zeidman, S. Levinson, S. Mukhopadhyay, R. E. Segel, B. Anderson, R. Madey, J. Watson, and R. R. Whitney, Phys. Rev. C **40**, 1347 (1989).

[4] P. Weber, G. Backenstoss, M. Izycki, R. J. Powers, P. Salvisberg, M. Steinacher, H. J. Weyer, S. Cierjacks, A. Hoffart, B. Rzehorz, H. Ullrich, D. Bosnar, M. Furić, T. Petković, and N. Šimičević, Nucl. Phys. **A534**, 541 (1991).

[5] S. Mukhopadhyay, S. Levenson, R. E. Segel, G. Garino, D. Geesaman, J. P. Schiffer, G. Stephans, B. Zeidman, E. Ungricht, H. Jackson, R. Kowalczyk, D. Ashery, E. Piasetsky, M. Moinester, I. Navon, L. C. Smith, R. C. Minehart, G. S. Das, R. R. Whitney, R. Mckeown, B. Anderson, R. Madey, and J. Watson, Phys. Rev. C **43**, 957 (1991).

[6] P. Salvisberg, G. Backenstoss, H. Krause, R. J. Powers, M. Steinacher, H. J. Weyer, M. Wildi, A. Hoffart, B. Rzehorz, H. Ullrich, D. Bosnar, M. Furić, T. Petković, N. Šimičević, H. Zmeskal, A. Janett, and R. H. Sherman, Phys. Rev. C **46**, 2172 (1992).

[7] T. Alteholz, D. Androić, G. Backenstoss, D. Bosnar, H. Breuer, A. Brković, H. Döbbeling, T. Dooling, W. Fong, M. Furić, P. A. M. Gram, N. K. Gregory, J. P. Haas, A. Hoffart, C. H. Q. Ingram, A. Klein, K. Koch, J. Köhler, B. Kotliński, M. Kroedel, G. Kyle, A. Lehmann, Z. N. Lin, G. Mahl, A. O. Mateos, K. Michaelian, S. Mukhopadhyay, T. Petković, R. P. Redwine, D. Rowntree, R. Schumacher, U. Sennhauser, N. Šimičević, F. D. Smit, G. van der Steenhoven, D. R. Tieger, R. Trezeciak, H. Ullrich, M. Wang, M. H. Wang, H. J. Weyer, M. Wildi, and K. E. Wilson, Phys. Rev. Lett. **73**, 1336 (1994).

[8] H. Hahn, A. Altman, D. Ashery, G. Gefen, D. R. Gill, R. R. Johnson, R. Levy-Nathansohn, M. A. Moinester, M. Sevior, and R. P. Trelle, Phys. Rev. C **53**, 1074 (1996).

[9] M. Steinacher, G. Backenstoss, M. Izycki, P. Salvisberg, P. Weber, H. J. Weyer, A. Hoffart, B. Rzehorz, H. Ullrich, M. Dzemidzić, M. Furić, and T. Petković, Nucl. Phys. **A517**, 413 (1990).

[10] P. Weber, J. McAlister, R. Olszewski, A. Feltham, M. Hanna, R. Johnson, M. Pavan, C. Ponting, F. Rozon, M. Sevior, V. Sossi, D. Vetterli, D. Humphrey, G. Lolos, Z. Papandreou, R. Tacik, D. Ottewell, G. Sheffer, G. Smith, Y. Mardor, and S. May-Tal, Phys. Rev. C **43**, 1553 (1991).

[11] C. H. Q. Ingram, Nucl. Phys. **A553**, 573c (1993).

[12] K. Ohta, M. Thies, and T. -S. H. Lee, Ann. Phys. (N.Y.) **163**, 420 (1985).
[13] H. J. Weyer, Phys. Rep. **195**, 295 (1990).
[14] G. Backenstoss, M. Izycki, R. Powers, P. Salvisberg, M. Steinacher, P. Weber, H. J. Weyer, A. Hoffart, B. Rzehorz, H. Ullrich, D. Bosnar, M. Furić, and T. Petković, Phys. Lett. B **222**, 7 (1989).
[15] G. Backenstoss, D. Bosnar, H. Breuer, H. Döbbeling, T. Dooling, M. Furić, P. A. M. Gram, N. K. Gregory, A. Hoffart, C. H. Q. Ingram, A. Klein, K. Koch, J. Köhler, B. Kotliński, M. Kroedel, G. Kyle, A. Lehmann, A. O. Mateos, K. Michaelian, T. Petković, R. P. Redwine, D. Rowntree, U. Sennhauser, N. Šimičević, R. Trezeciak, H. Ullrich, M. Wang, M. H. Wang, H. J. Weyer, M. Wildi, and K. E. Wilson, Phys. Lett. B **379**, 60 (1996).
[16] D. Androić, G. Backenstoss, D. Bosnar, H. Breuer, H. Döbbeling, T. Dooling, M. Furić, P. A. M. Gram, N. K. Gregory, A. Hoffart, C. H. Q. Ingram, A. Klein, K. Koch, J. Köhler, B. Kotliński, M. Kroedel, G. Kyle, A. Lehmann, A. O. Mateos, K. Michaelian, T. Petković, R. P. Redwine, D. Rowntree, U. Sennhauser, N. Šimičević, R. Trezeciak, H. Ullrich, M. Wang, M. H. Wang, H. J. Weyer, M. Wildi, and K. E. Wilson, Phys. Rev. C **53**, R2591 (1996).
[17] V. M. Kolybasov, Sov. J. Nucl. Phys. **3**, 535 (1966); **3**, 704 (1966); V. M. Kolybasov and T. A. Lomonosova, *ibid.* **11**, 325 (1970); V. M. Kolybasov and V. A. Tsepov, *ibid.* **14**, 418 (1972).
[18] G. E. Brown, H. Toki, W. Weise, and A. Wirzba, Phys. Lett. **118B**, 39 (1982); B. Schwesinger, A. Wirzba, and G. E. Brown, *ibid.* **132B**, 269 (1983).
[19] E. Oset, Y. Futami, and H. Toki, Nucl. Phys. **A448**, 597 (1986).
[20] C. Fasano and T.-S. H. Lee, Phys. Lett. B **217**, 9 (1989).
[21] T. Alteholz, D. Androić, G. Backenstoss, D. Bosnar, H. Breuer, A. Brković, H. Döbbeling, T. Dooling, W. Fong, M. Furić, P. A. M. Gram, N. K. Gregory, J. P. Haas, A. Hoffart, C. H. Q. Ingram, A. Klein, K. Koch, J. Köhler, B. Kotliński, M. Kroedel, G. Kyle, A. Lehmann, Z. N. Lin, G. Mahl, A. O. Mateos, K. Michaelian, S. Mukhopadhyay, T. Petković, M. Planinić, R. P. Redwine, D. Rowntree, R. Schumacher, U. Sennhauser, N. Šimičević, F. D. Smit, G. van der Steenhoven, D. R. Tieger, R. Trezeciak, H. Ullrich, M. Wang, M. H. Wang, H. J. Weyer, M. Wildi, and K. E. Wilson, Nucl. Instrum. Methods Phys. Res. A **373**, 374 (1996).
[22] K. Gottfried and J. D. Jackson, Nuovo Cimento **33**, 309 (1964).
[23] J. Werle, *Relativistic Theory of Reactions* (North-Holland, Amsterdam, 1966)
[24] A.M. Baldin, V.I. Goldanskii, V.M. Maksimenko, and I.L. Rosental, *Kinematika Jadernih Reaktsii* (Atomizdat, Moscow, 1968).
[25] A. Mateos, Ph.D. thesis, MIT Cambridge, 1995; A. Mateos *et al.*, unpublished.
[26] R. Trezeciak, Ph.D. thesis, University of Karlsruhe, 1995.
[27] J. Köhler, Ph.D. thesis, University of Basel, in preparation.
[28] N. Šimičević and A. Mateos, Phys. Rev. C **51**, 797 (1995).
[29] Y. Wu, S. Ishikawa and T. Sasakawa, Few-Body Syst. **15**, 145 (1993); S. Ishikawa and Y. Wu, private communication.
[30] E. Jans, P. Barreau, M. Bernheim, J. M. Finn, J. Morgenstern, J. Mougey, D. Tarnowski, S. Turck-Chieze, S. Frullani, F. Garibaldi, G. P. Capitani, E. de Sanctis, M. K. Brussel, and I. Sick, Phys. Rev. Lett. **49**, 974 (1982).
[31] B. G. Ritchie, Phys. Rev. C **44**, 533 (1991).
[32] SCATPI, J.B. Walter and G.A. Rebka, Los Alamos National Laboratory Report LA-7731-MS, 1979.
[33] R. A. Arndt, L. D. Roper, R. A. Bryan, R. B. Clark, B. J. VerWest, and P. Signell, Phys. Rev. D **28**, 97 (1983); R. A. Arndt, L. D. Roper, R. L. Workman, and M. W. McNaughton, *ibid.* **45**, 3995 (1992); SAID, R.A. Arndt *et al.*, Virginia Polytechnic Institute (1988).
[34] R. Schiavilla, V. R. Pandharipande, and R. B. Wiringa, Nucl. Phys. **A449**, 219 (1986).
[35] R. Schiavilla, private communication.
[36] J. F. J. van den Brand, H. P. Blok, R. Ent, E. Jans, J. M. Laget, L. Lapikás, C. de Vries, and P. K. A. de Witt Huberts, Nucl. Phys. **A534**, 637 (1991).
[37] J. Gillespie, *Final-State Interactions* (Holden-Day, San Francisco, 1965).
[38] B. Zeitnitz, R. Maschuw, and P. Suhr, Nucl. Phys. **A149**, 449 (1970).
[39] R. Taylor, *Scattering Theory* (Wiley, New York, 1972), pp. 424–432.
[40] K. Watson, Phys. Rev. **88**, 1163 (1952); A.B. Migdal, Sov. Phys. JETP **1**, 2 (1955); M.L. Goldberger and K.M. Watson, *Collision Theory* (Wiley, New York, 1964).
[41] L. Salcedo, E. Oset, and D. Strottman, Phys. Lett. B **208**, 339 (1988).
[42] M. Planinić, Ph.D. thesis, University of Zagreb, in preparation.
[43] K. Wilson, Ph.D. thesis, MIT Cambridge, 1995.
[44] H. Kamada, private communication.